Supporting Information

for

Diemissive Dye@CP composites with full-spectrum tunable mechanoluminescence

Jiaxiang Huang,[a b] He Zhao,[b] Jian-Jun Zhang,*[a,b] Bo-Lun Zhang,[b] Jun Ni ,[b] Bo Song,*[b] Yan-Qin Li,*[b] Shuqin Liu[b] and Chunying Duan*[a c]

[a] *State Key Laboratory of Fine Chemicals, Dalian University of Technology, Dalian, 116024, China*

[b] *School of Chemical Engineering, Dalian University of Technology, Dalian 116024, China*

[c] *Zhang Dayu College of Chemistry, Dalian University of Technology, Dalian, 116024, China*

*Corresponding authors. zhangjj@dlut.edu.cn (J.-J. Zhang); bo.song@dlut.edu.cn (B. Song); cyduan@dlut.edu.cn (C.-Y. Duan)

1. Experimental Procedures

1.1. Materials and physical measurements

All commercially available reagents and solvents were used as received without further purification. Infrared spectra (IR) were recorded on Nicolet-6700 spectrometer in the range of 4000−400 cm^{-1}. ESI mass spectra were recorded using a LCQ-Tof MS mass spectrometer (Samples were deprotonated using NaAc). NMR spectra were recorded at ambient temperature on a Bruker Avance II 400M spectrometer. Thermogravimetric analyses (TGAs) were performed under nitrogen atmosphere with a heating rate of 10 °C/min using a TA-Q50 thermogravimetric analyzer. Elemental analyses of C, H, and N were determined on a Vario EL Ⅲ Elemental Analyzer. Powder X-ray diffraction patterns (PXRD) data were collected on a D/MAX-2400 X-ray Diffractometer. Luminescent spectra were acquired at ambient temperature by using a Hitachi F-7000 fluorescence spectrophotometer. The laser confocal scanning analysis was obtained with an Olympus FV1000 single-photon laser confocal microscope. H_2L was synthesized according to reported method.[1]

*1.2. Synthesis of [CdL(DMF)$_2$] (**1**)*

A mixture containing 0.02 mmol H_2L and 0.015 mmol $Cd(NO_3)_2 \cdot 4H_2O$ in DMF/H_2O (2mL/0.5mL) in a 20 mL scintillation vial was heated at 105 ºC for 2 d and then cooled to room temperature. The colorless crystals were collected, washed with DMF and dried in air (66.7% yield). Element analysis (%) calcd for $C_{26}H_{23}CdN_3O_8$: C, 50.54; H, 3.75; N, 6.80. Found: C, 50.35; H, 3.39; N, 6.61. IR (cm^{-1}): 3356(w,b), 2930(w), 1979(w), 1706(m), 1644(s), 1568(s), 1436(m), 1370(s), 1296(m), 1238(s), 1192(m), 1154(w), 1106(m), 1026(w), 843(m), 812(w), 771(s), 673(m).

*1.3. Synthesis of [CdL(H$_2$O)$_3$]·H$_2$O (**2**)*

50 mg **1** (0.092 mmol) was soaked in 15 mL H_2O in a 20 mL scintillation vial and kept at room

temperature for 2 d. The colorless crystals were collected, washed with H_2O and dried in air (55.4 % yield). Element analysis (%) calcd for $C_{20}H_{17}CdNO_{10}$: C, 44.18; H, 3.15; N, 2.58. Found: C, 44.25; H, 3.21; N, 2.61. IR (cm^{-1}): 3441(s), 3315(m), 3206(m), 2160(w), 1695(m), 1649(s), 1622(w), 1532(s), 1372(s), 1293(m), 1242(s), 1154(w), 1071(w), 915(w), 845(m), 771(s), 656(s).

*1.4. Synthesis of dye@**2** composites*

A mixture in a 20 mL scintillation vial was prepared by mixing 50 mg (0.092 mmol) compound **1** and dyes of systematically varied concentrations (For example, 0.15 mmol, 0.075 mmol, 0.015 mmol, 0.0075 mmol and 0.0015 mmol phloxine B for the preparation of PhB1@**2**, PhB2@**2**, PhB3@**2**, PhB4@**2** and PhB5@**2** respectively) in 15 mL H_2O. Then the mixture was left in the dark for 2 days. The obtained crystals were washed several times with H_2O until no characteristic emission of dye was observed in the filtrate upon excitation, and dried in the air for further characterization.

1.5. X-ray Crystallographic Study

The intensity data of single crystals was measured at 293 (2) K (for **1**) 150 (2) K (for **2**) on a Bruker SMART APEX II CCD area detector system. Data were corrected for absorption effects using the multi-scan technique (SADABS). The structure was solved by direct methods using SHELXS-2014 and was refined by full-matrix least squares methods using SHELXS-2014.[2] The hydrogen atoms were included in the structural model as fixed atoms "riding" on their respective carbon atoms using the idealized sp^2-hybridized geometry and C–H bond lengths of 0.95Å. No attempts were made to locate the hydrogen atoms on the coordinated H_2O.

A summary of the most important crystal and structure refinement data is given in Table S1. CCDC 2077561-2077562 contains the supplementary crystallographic data for this paper. The data can be obtained free of charge via www.ccdc.cam.ac.uk/conts/retrieving.html (or from the Cambridge

Crystallographic Data Centre, 12 Union Road, Cambridge CB2 1EZ, UK; fax: (+44) 1223-336-033; or e-mail: deposit@ccdc.cam.ac.uk).

2. *Supplementary Figures*

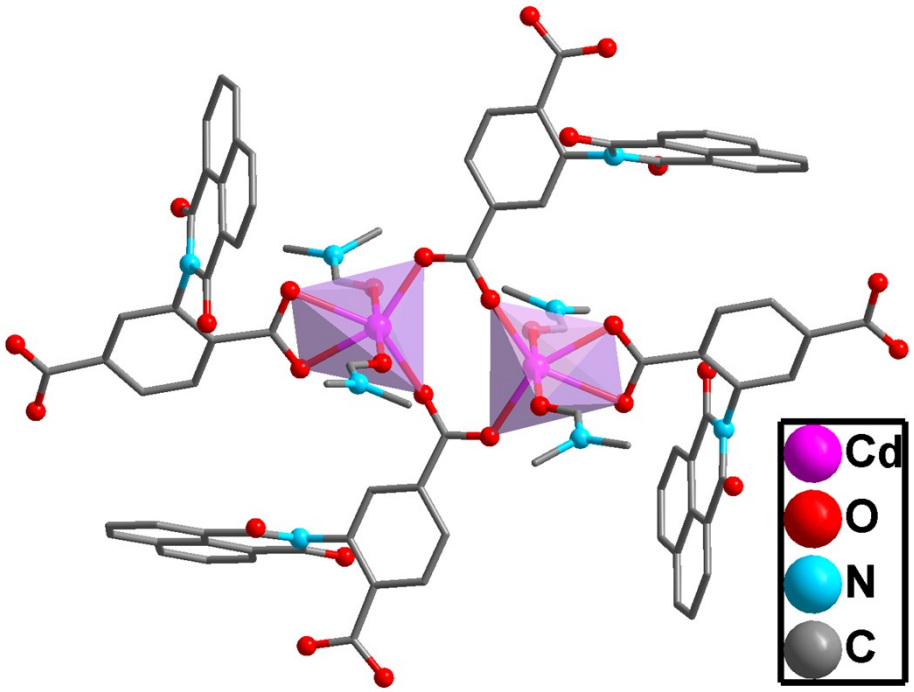

Fig. S1. The coordination environment of the metal ion in compound **1**.

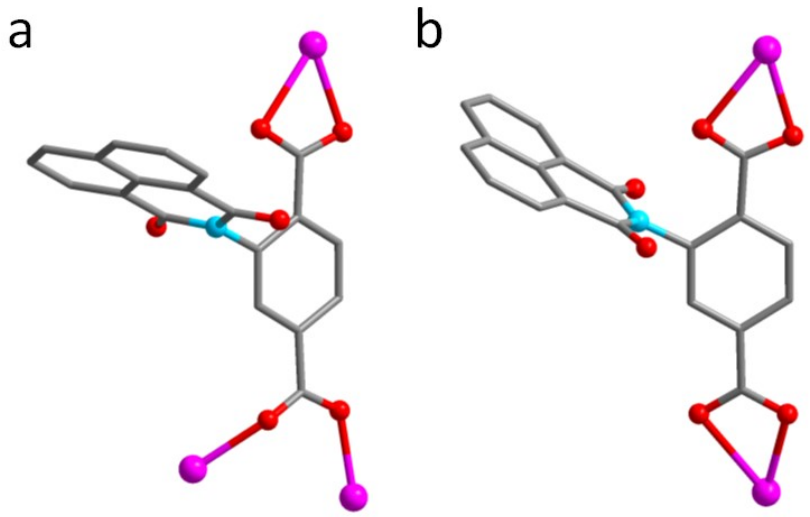

Fig. S2. The two coordination modes of ligands in the two compounds.

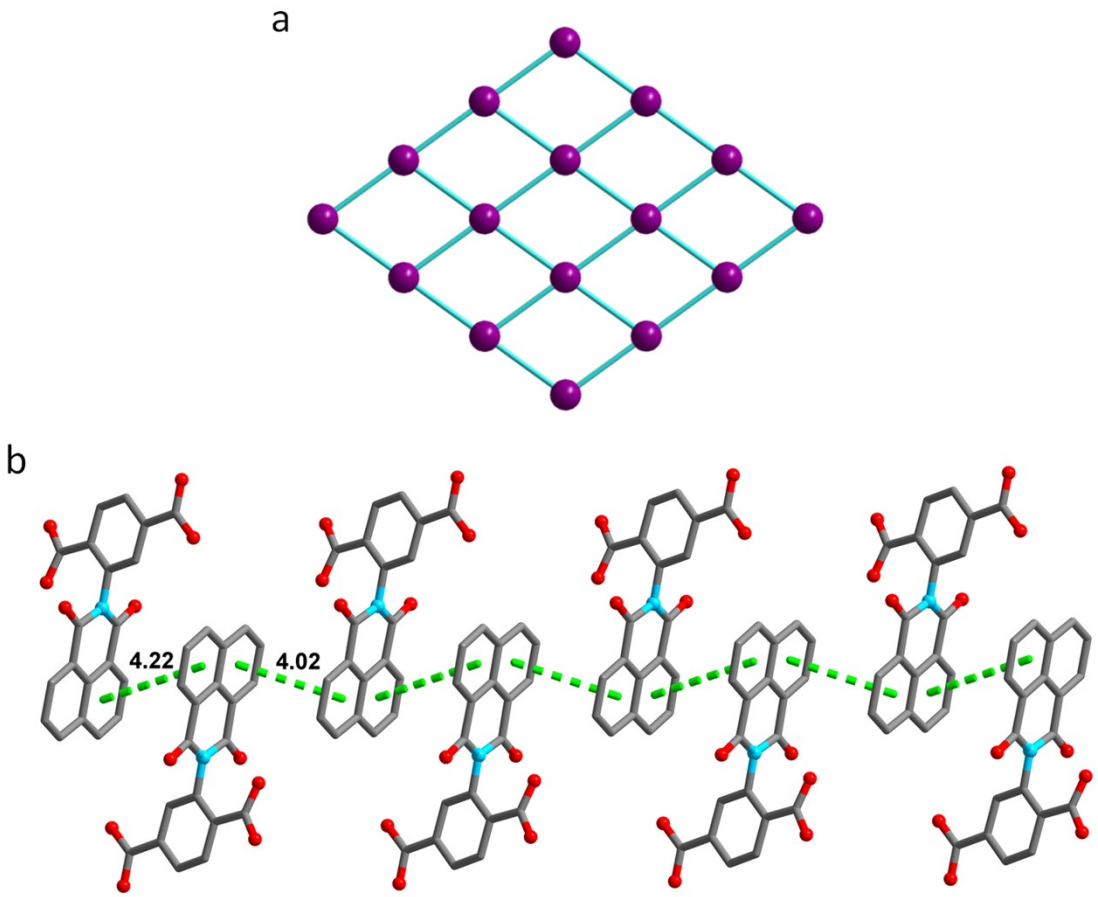

Fig. S3. (a) The framework topology of the 2D net of **1**. (b) The π-π interactions (represented as green dotted lines) between neighboring ligands in the structure of **1**.

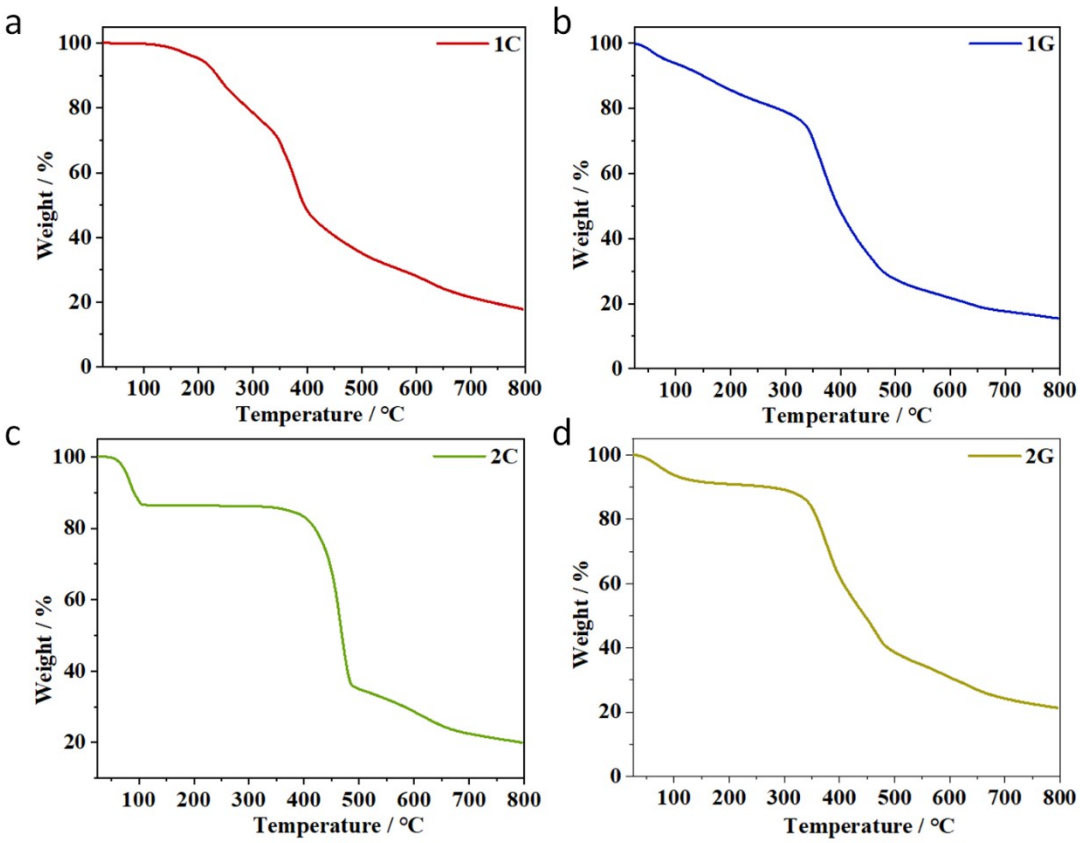

Fig. S4. Thermogravimetric analysis (TGA) curves of the fresh and ground samples for **1** ((a) and (b)) and **2** ((c) and (d)) respectively.

Note: The thermal behavior of **1** involves loss of all the DMF solvent molecules before 315°C (exp. 24.05%; calc. 23.66%). Then the compound continues to lose weight until complete decomposition of the structure. The first step (13.48%) of weight loss of **2** occurs at temperatures below 108 °C and is assigned to the loss of all the H_2O solvent molecules (calc. 13.24%). Then there is a plateau in the temperature range of 108~348°C. After 400°C **2** shows a striking weight loss, indicating the complete decomposition of the structure.

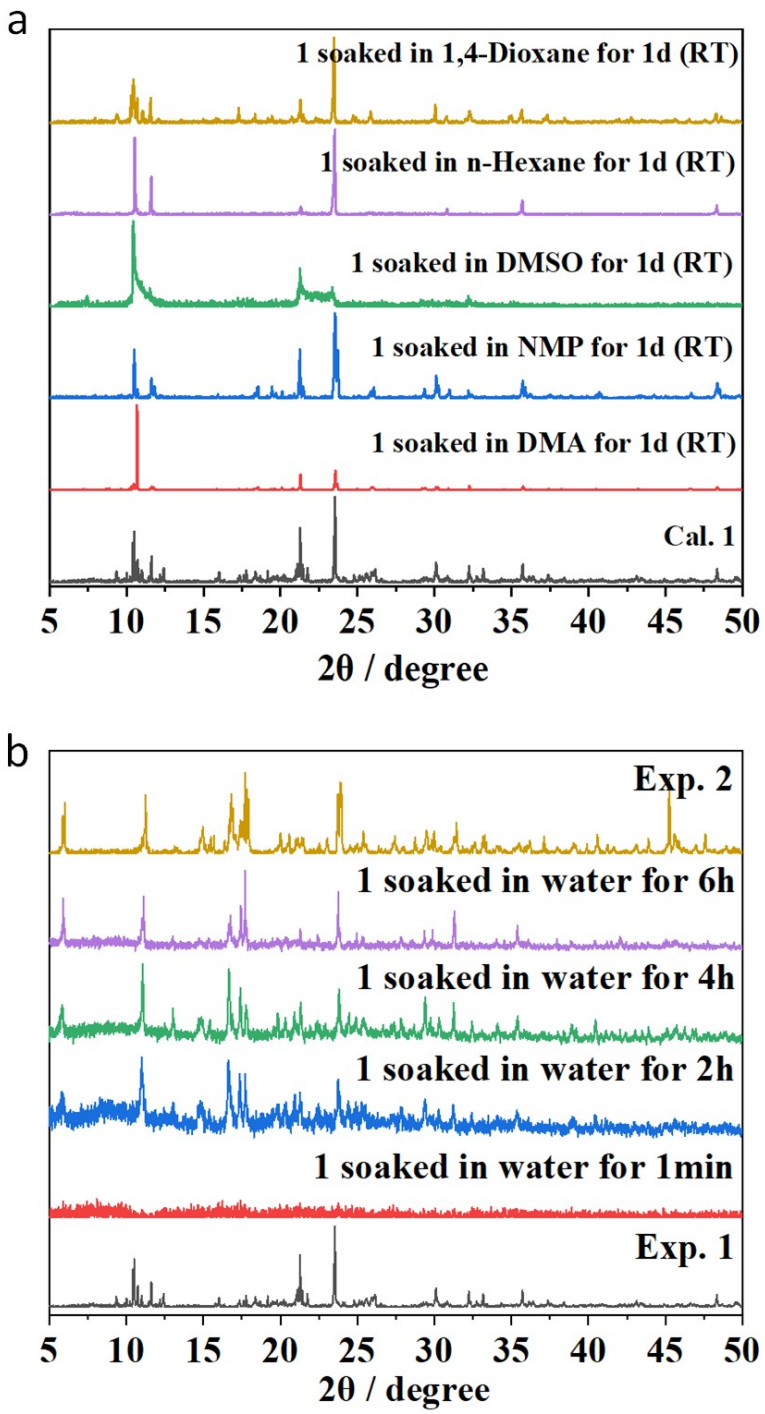

Fig. S5. (a) PXRD analyses indicate that **1** retains its framework when being soaked in several common organic solvents at room temperature. (b) PXRD of **1** after being soaked in water for different time.

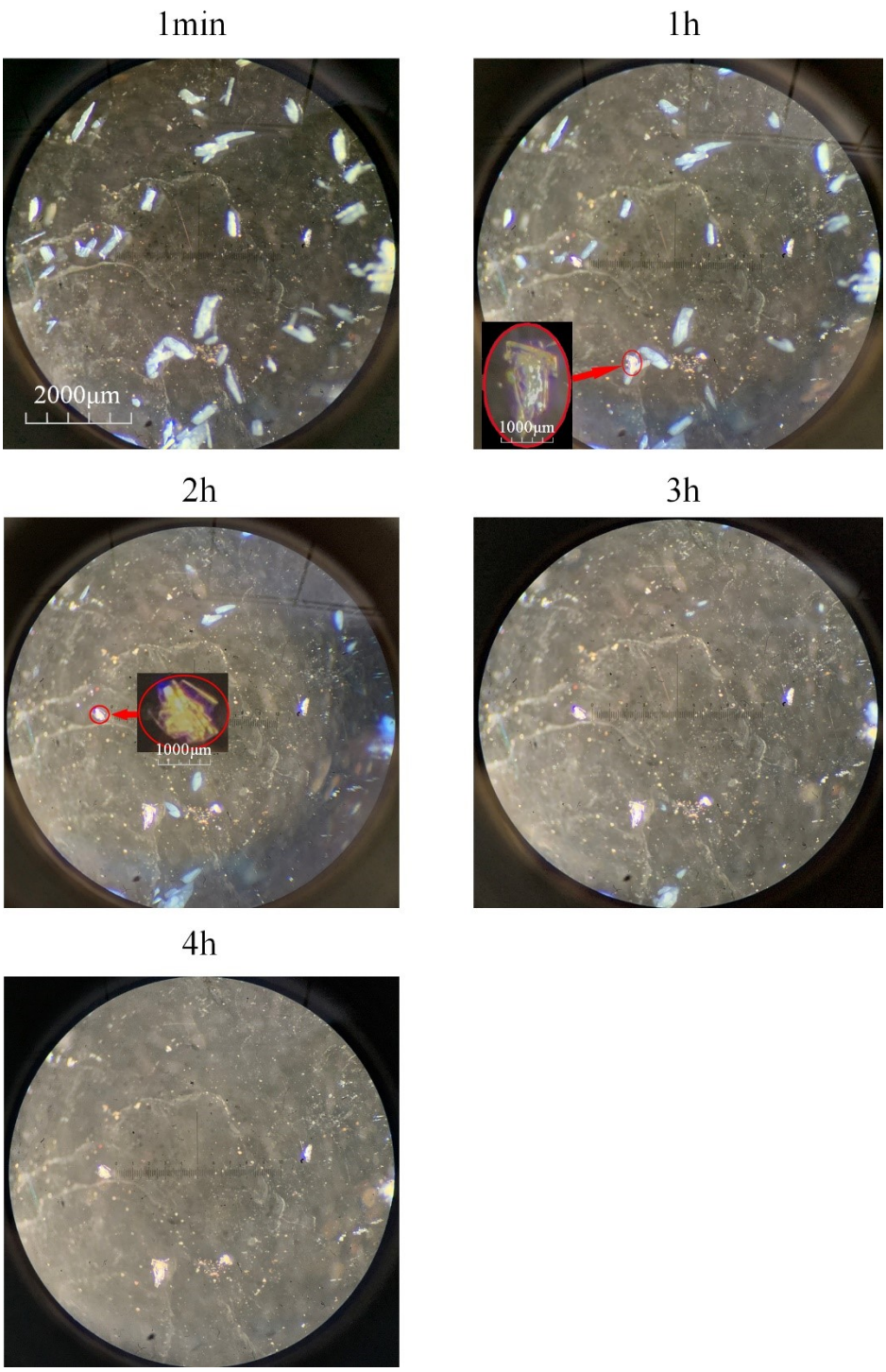

Fig. S6. An *in situ* microscopic observation of the conversion process of **1** to **2** (The newly formed compound **2** is in the red circle).

Note: During the transformation process, compound **1** first became transparent and then disappeared. Compound **2** started to form after 2 hours.

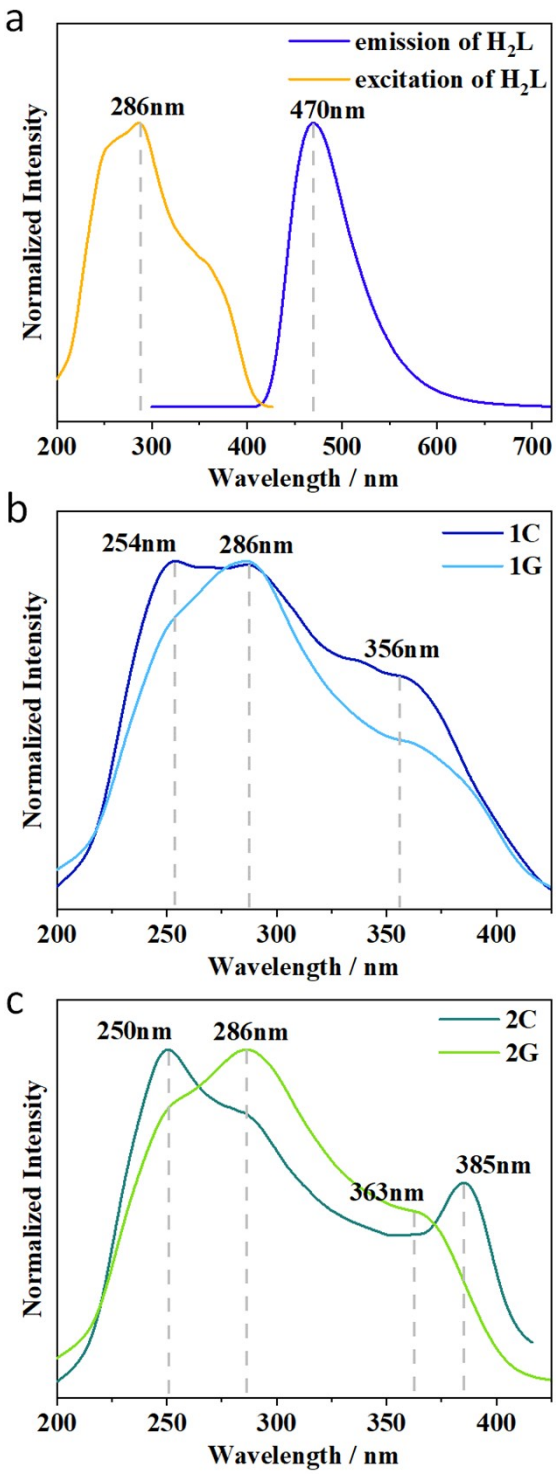

Fig. S7. (a) The solid state excitation (λ_{em} = 470 nm) and emission (λ_{ex} = 286 nm) spectra of H_2L. Normalized excitation spectra of the fresh and ground samples for **1** (b) (**1C**, λ_{em} = 452 nm; **1G**, λ_{em} = 470 nm), and **2** (c) (**2C**, λ_{em} = 456 nm; **2G**, λ_{em} = 484 nm).

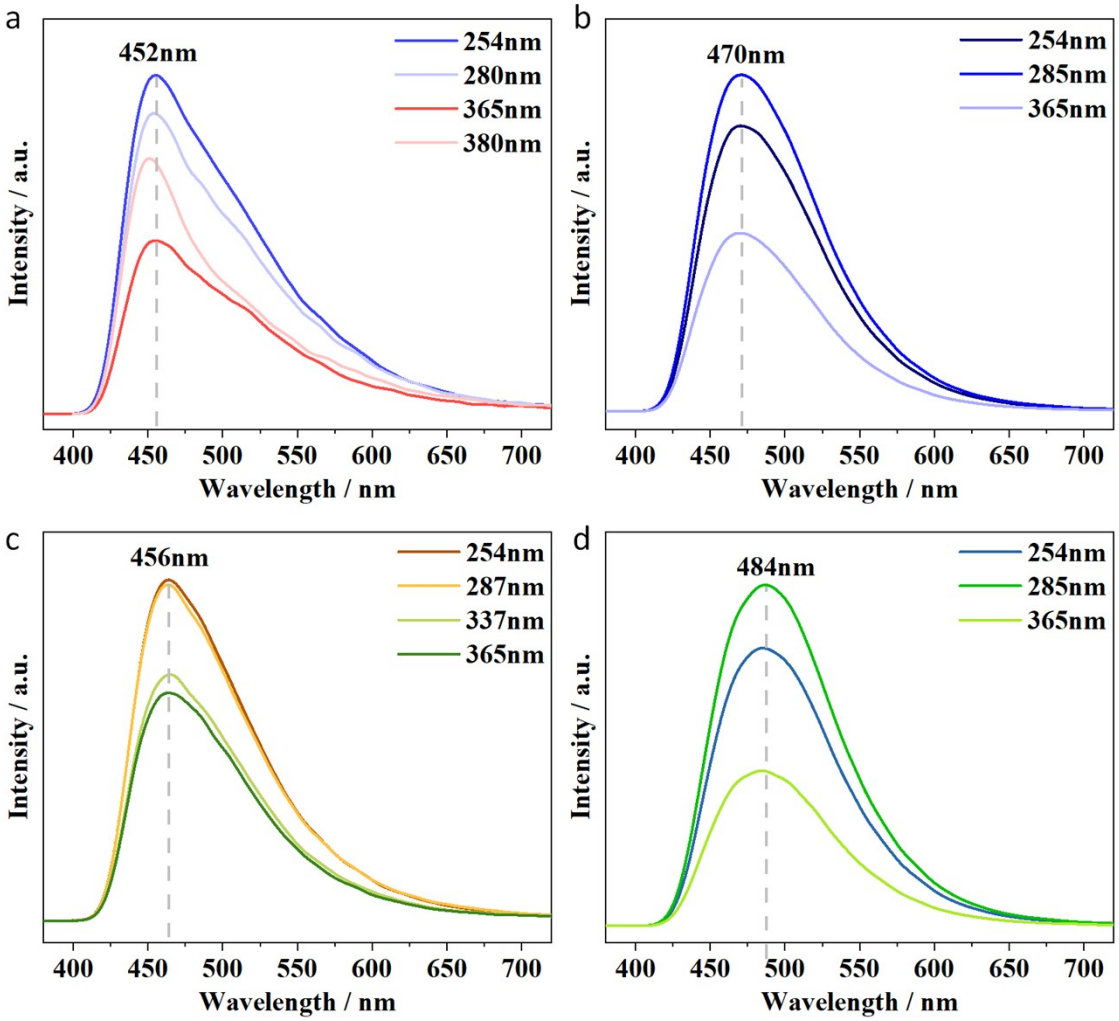

Fig. S8. The solid state emission spectra of **1C** (a), **1G** (b), **2C** (c) and **2G** (d) under different excitation wavelength.

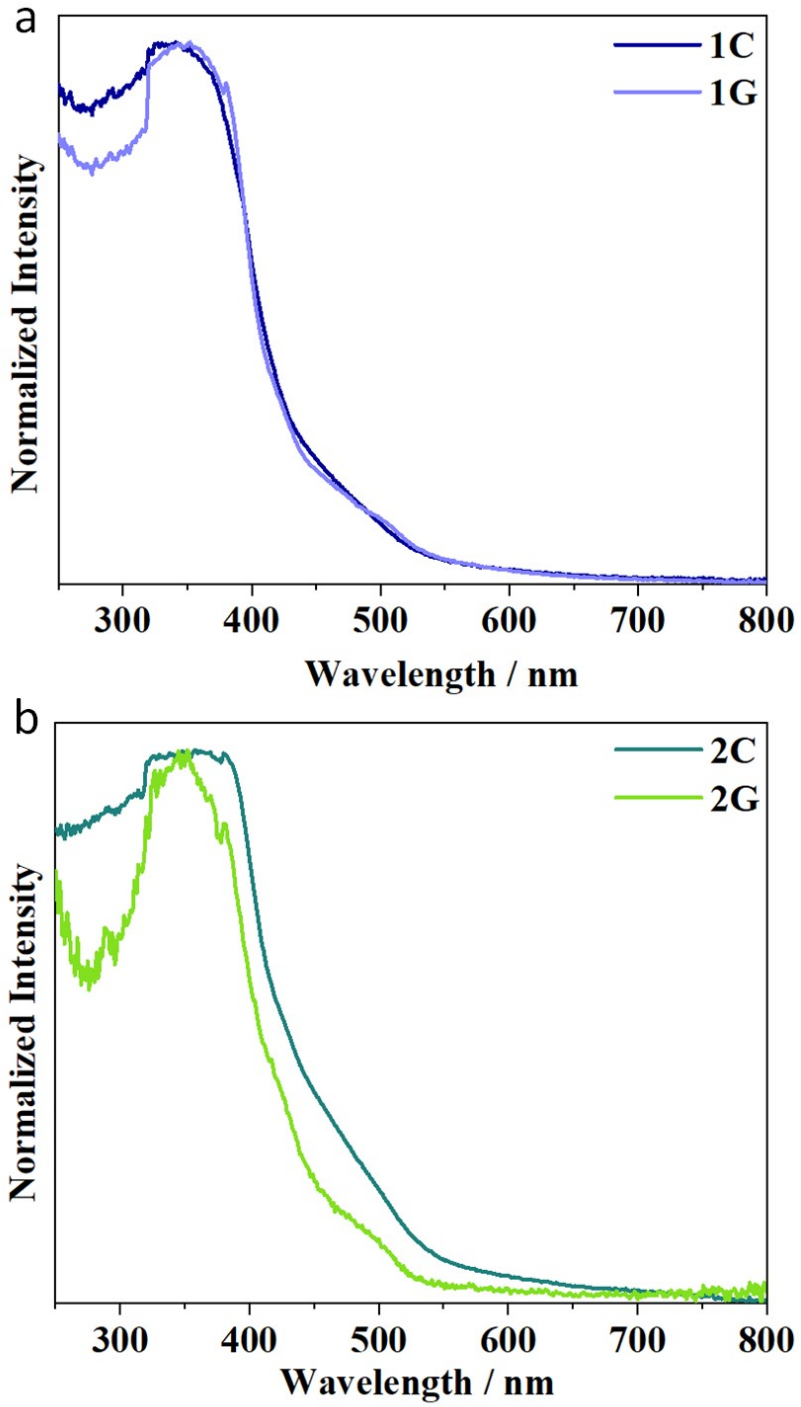

Fig. S9. The UV-Vis diffuse reflectance spectra of the fresh and ground samples for **1** (a) and **2** (b) respectively.

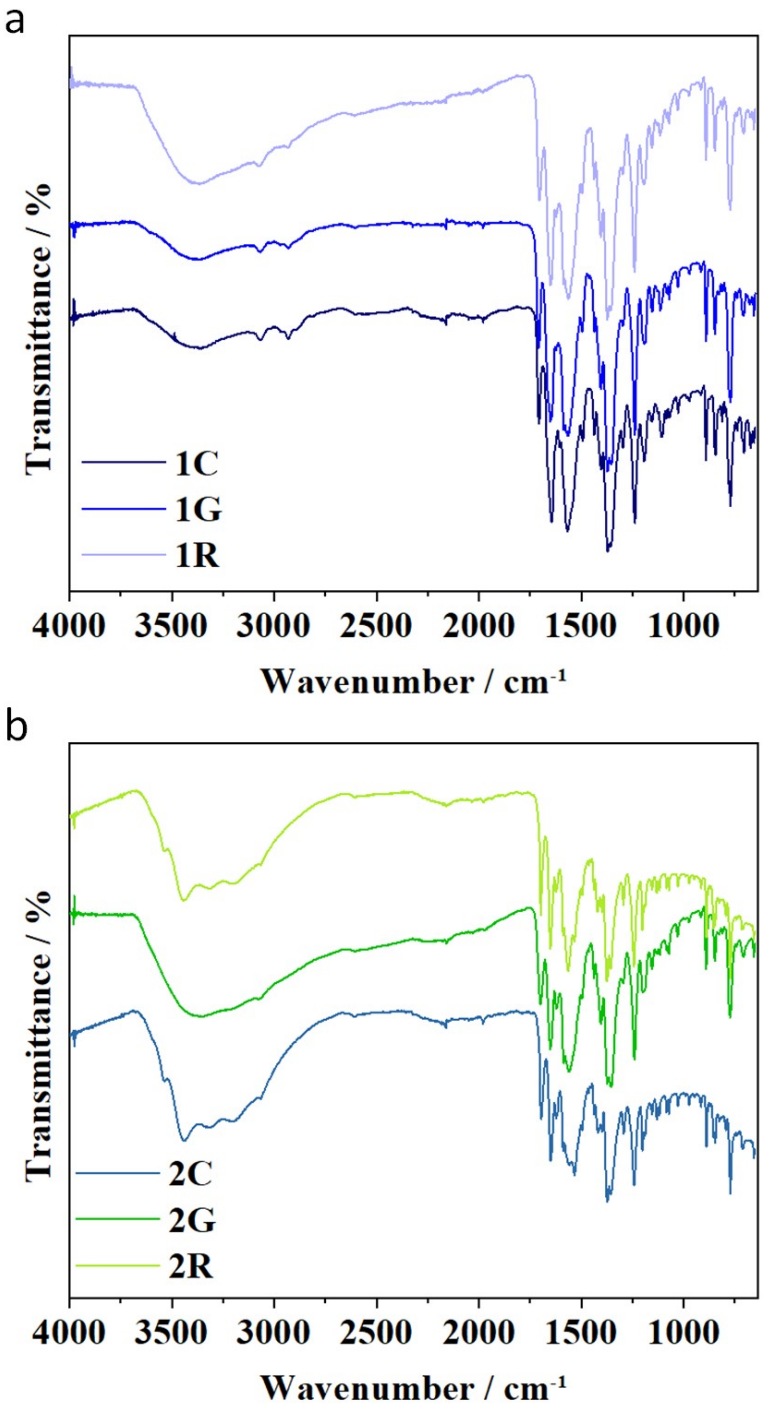

Fig. S10. IR spectra of **1** (a) and **2** (b) during the reversible MCL process.

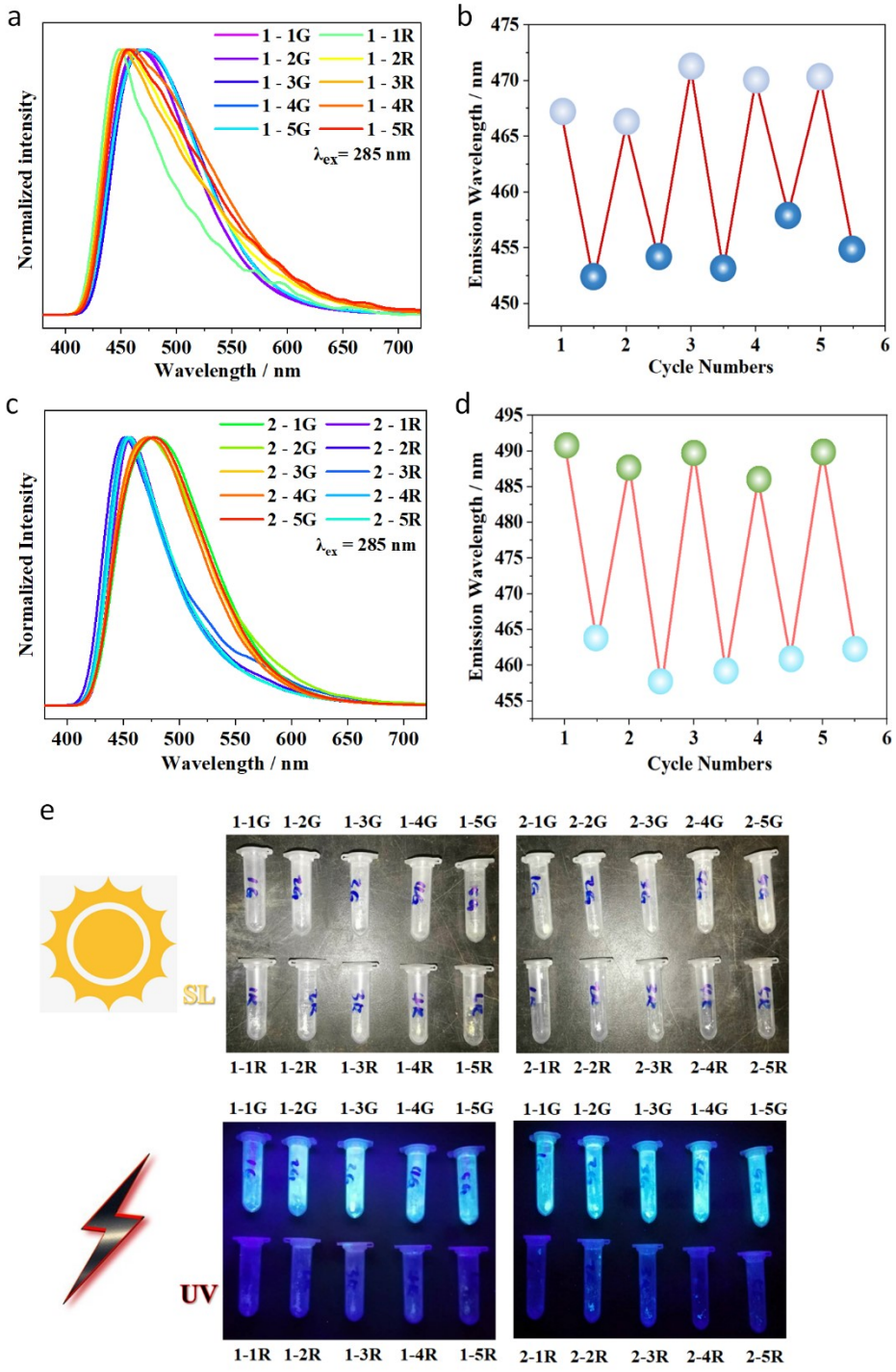

Fig. S11. Reversible grinding-fuming process of the photoluminescence (PL) of **1** (a and b)and **2** (c and d) (λ_{ex}= 285 nm) under alternate treatment of grinding and fuming by DMF (for **1**) or H_2O (for **2**). (f) The corresponding PL photographs under sunlight and a 365 nm UV lamp. (**G** stands for grinding phase, **R** stands for recovery phase)

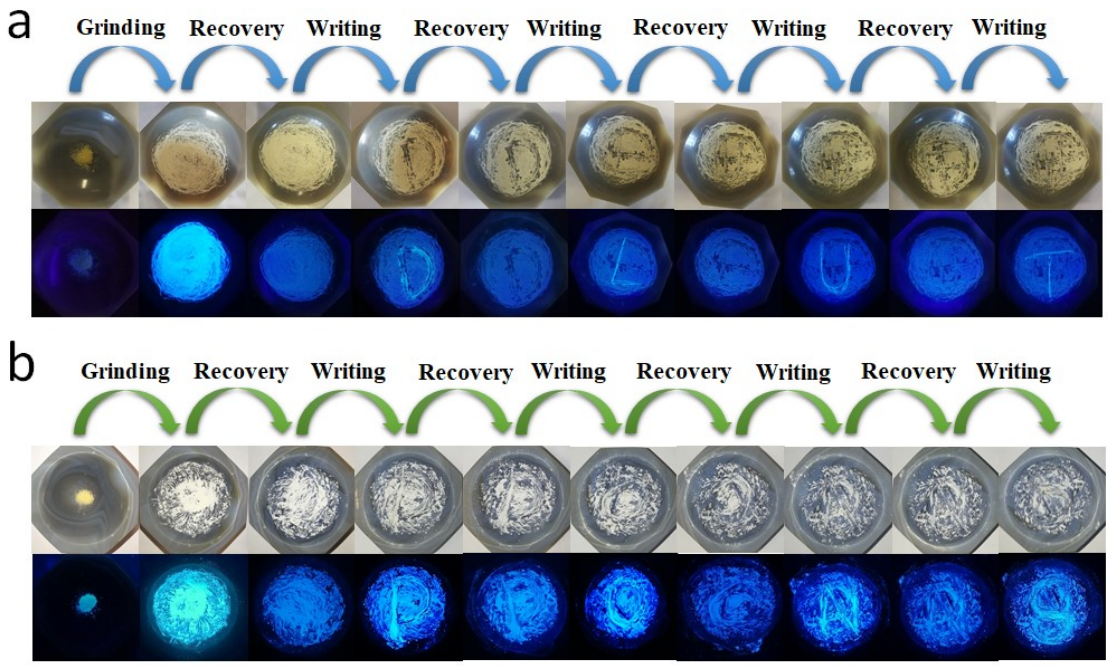

Fig. S12. Photographs of **1** (a) and **2** (b) upon grinding and fuming by DMF (for **1**) / H_2O (for **2**) vapors for several cycles under daylight and a 365 nm UV lamp.

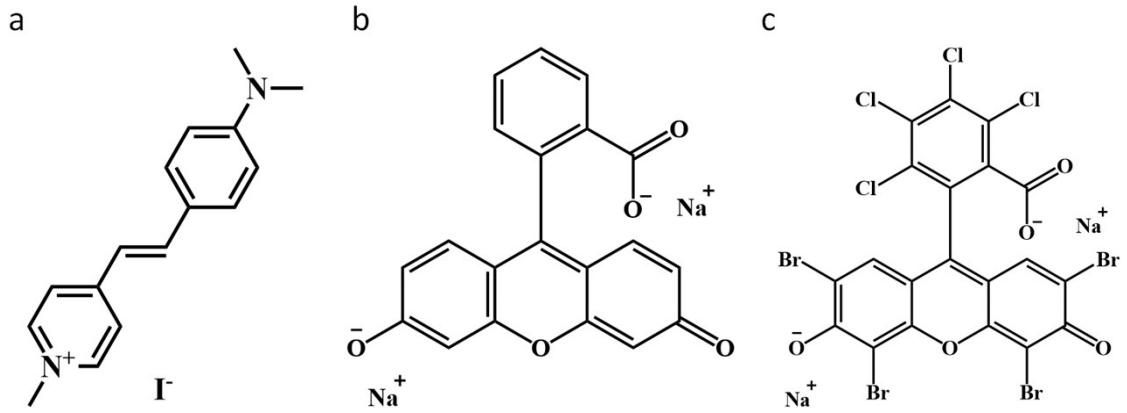

Fig. S13. The structures of the dyes used in this paper. (a) DSMI. (b) FRS. (c) PhB.

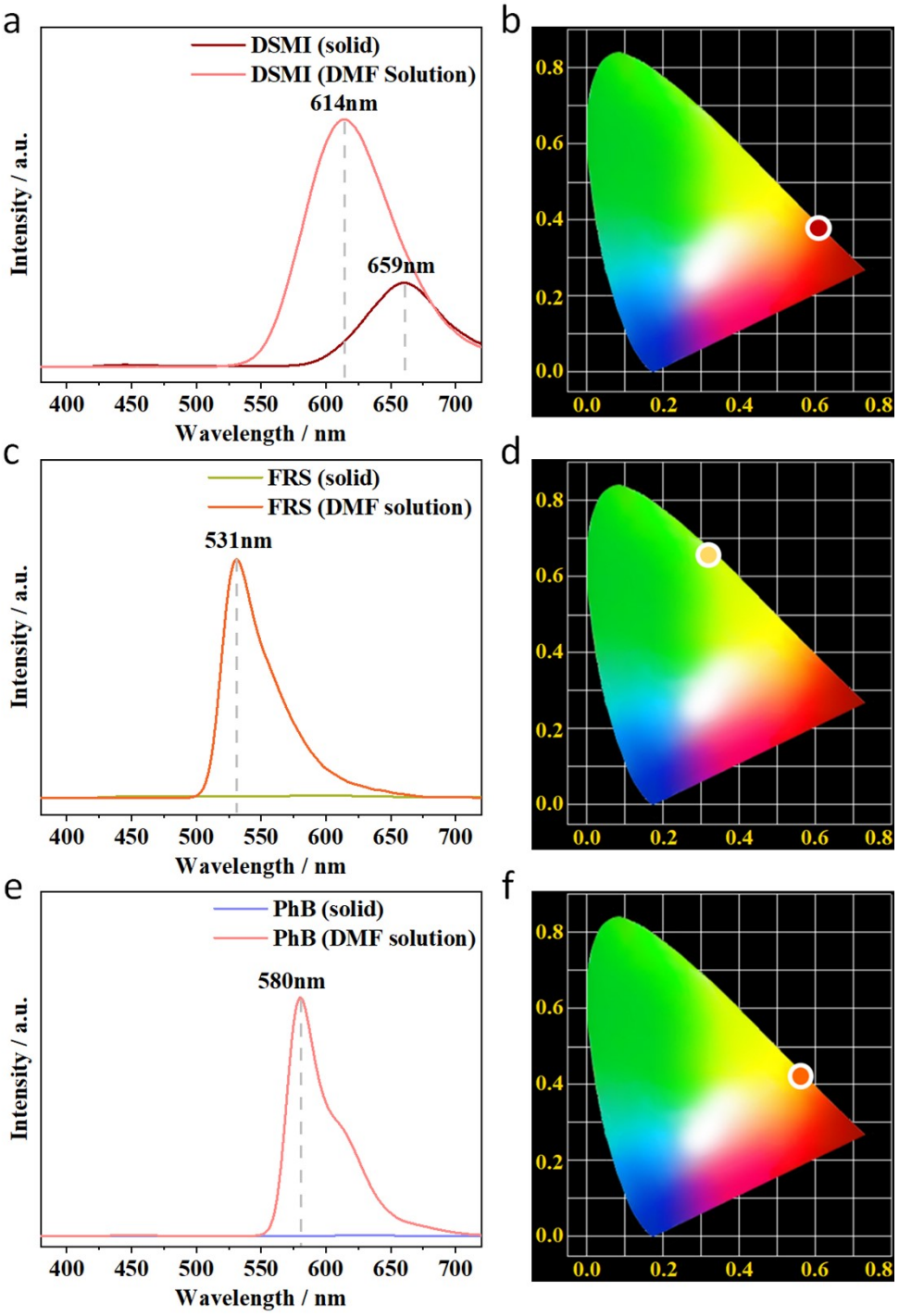

Fig. S14. Luminescent spectra of DSMI (a), FRS (c) and PhB (e) in the solid state and in DMF solution (λ_{ex} = 365 nm). CIE chromaticity coordinates of DSMI (b), FRS (d) and PhB (f) in DMF solution.

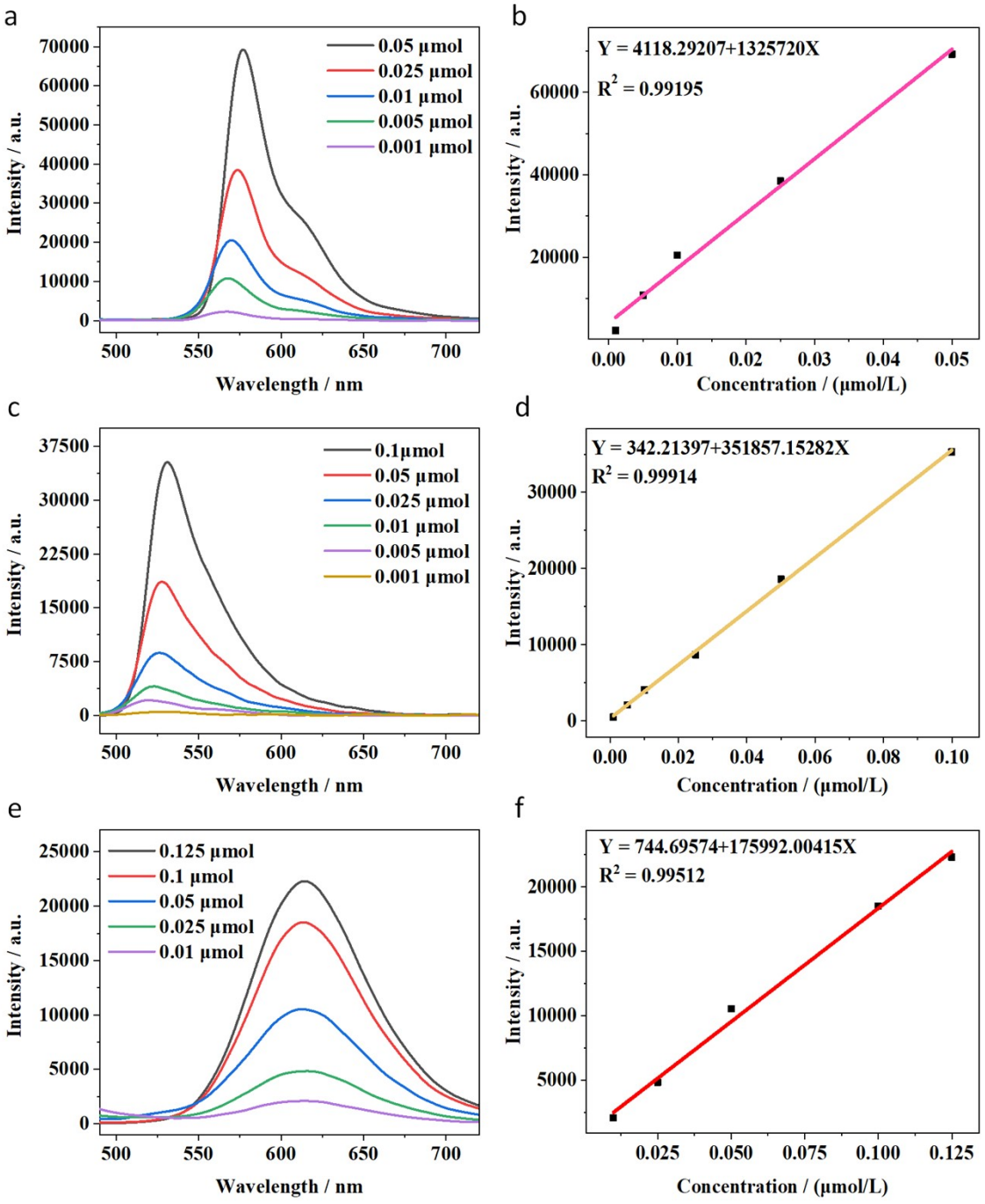

Fig. S15. Luminescent spectra of H_2O:DMF (v/v = 1:1) solutions of PhB (a), FRS (c) and DSMI (e) at different concentrations at room temperature (λ_{ex} = 365 nm). The luminescence intensity-concentration relationship for PhB (b), FRS (d) and DSMI (f) in H_2O:DMF (v/v = 1:1) solution.

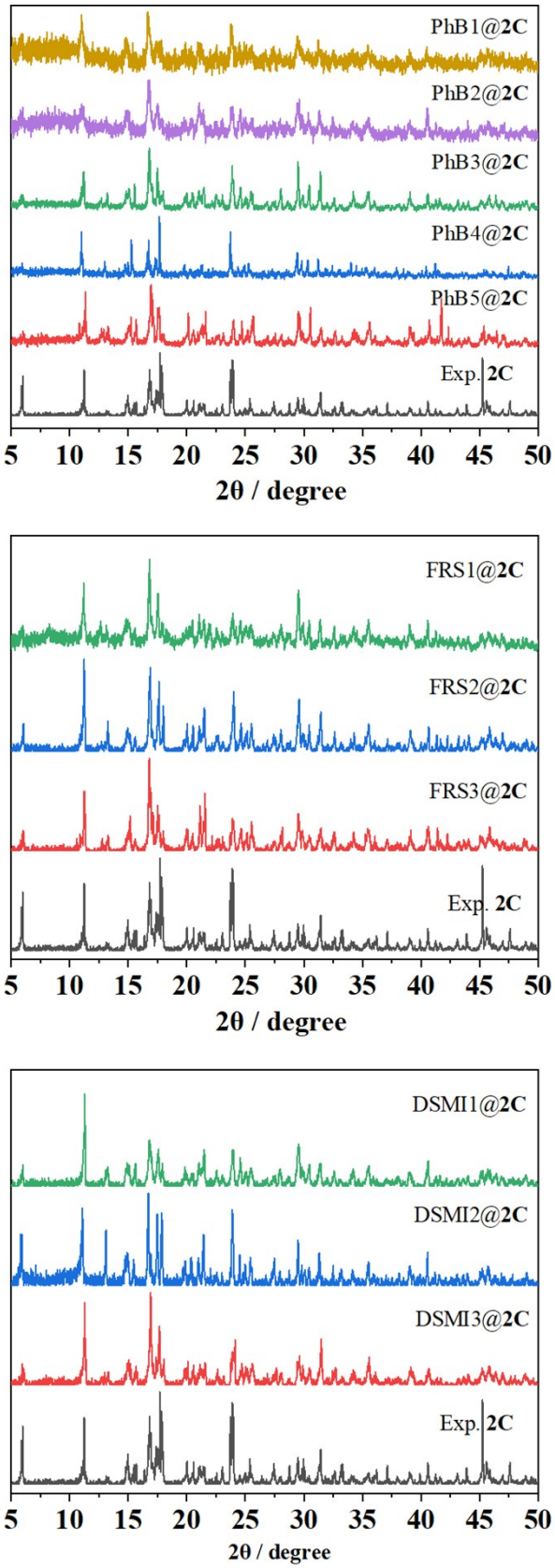

Fig. S16. PXRD patterns of the dye@**2** composites.

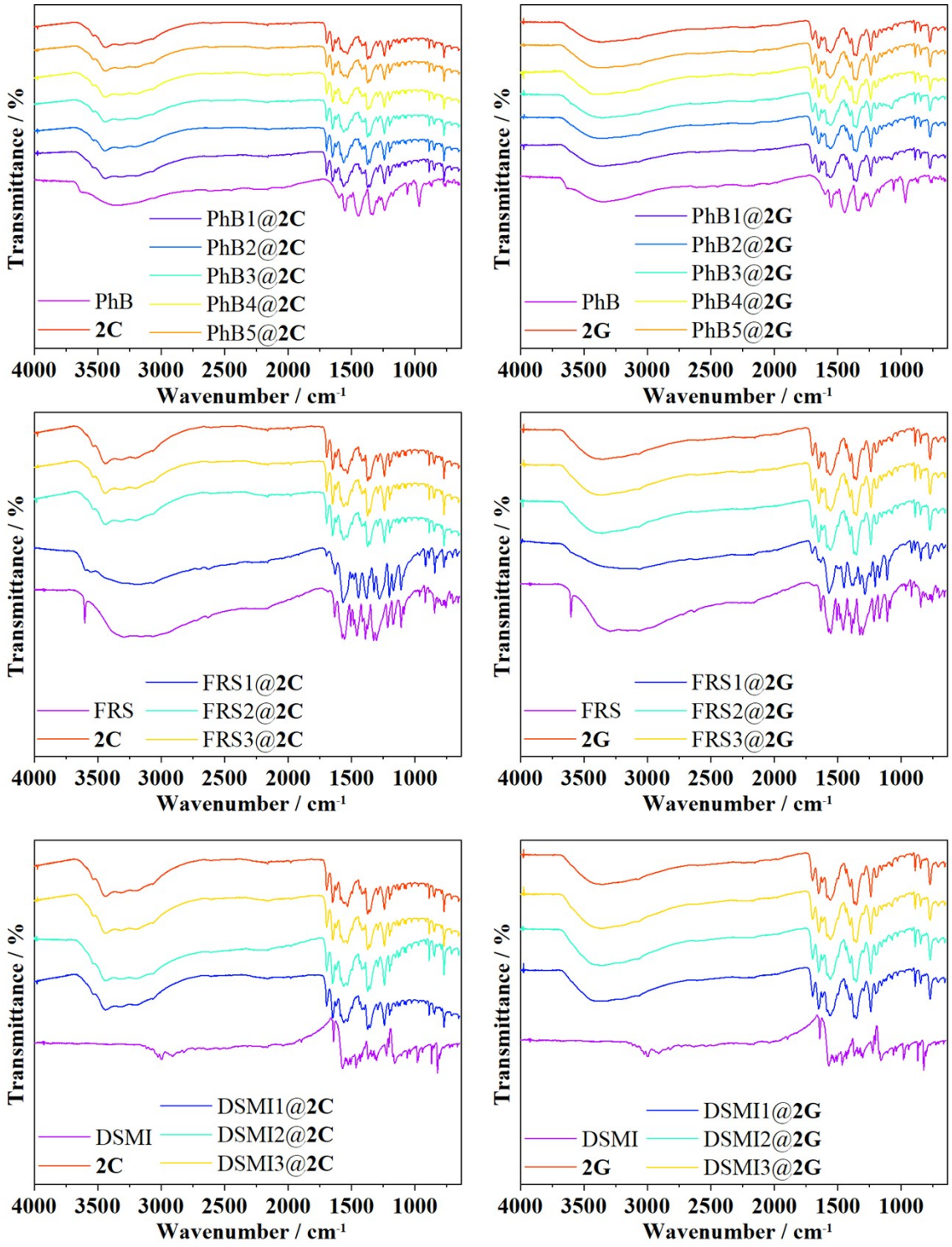

Fig. S17. IR spectra of the dye@**2** composites.

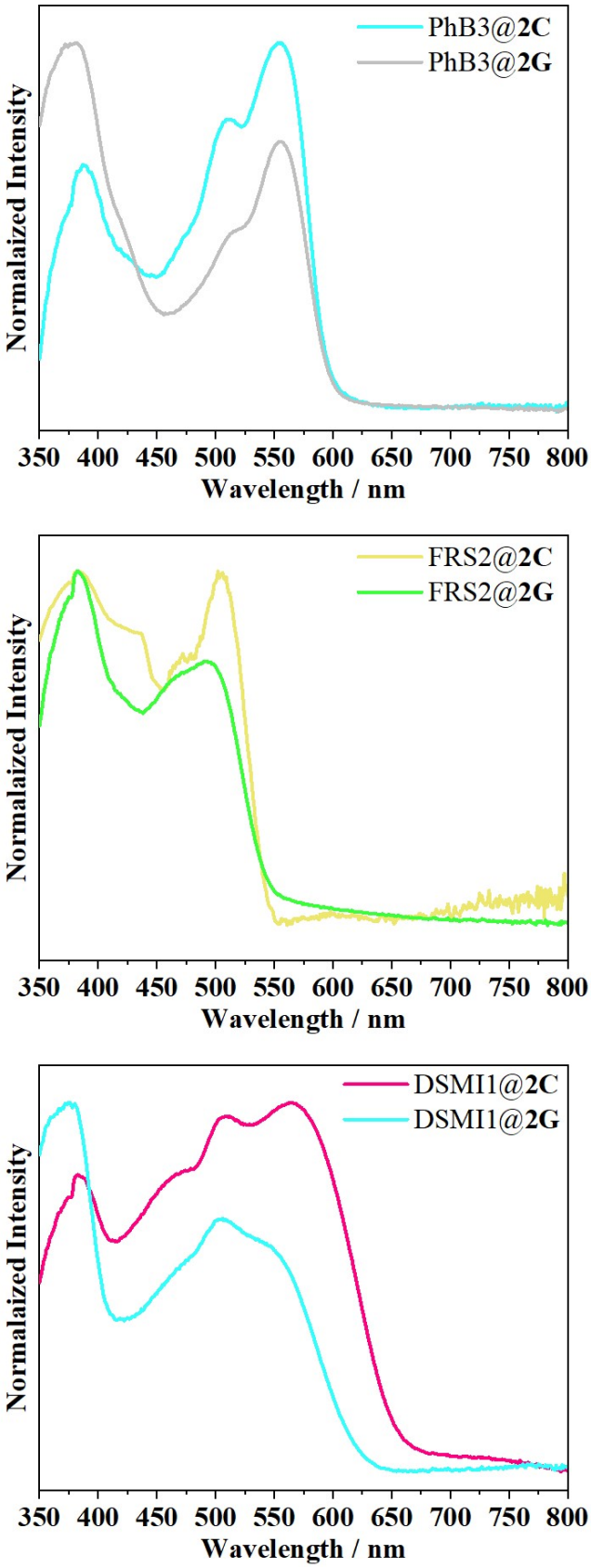

Fig. S18. The UV-Vis diffuse reflectance spectra of the fresh and ground samples for dye@**2** composites.

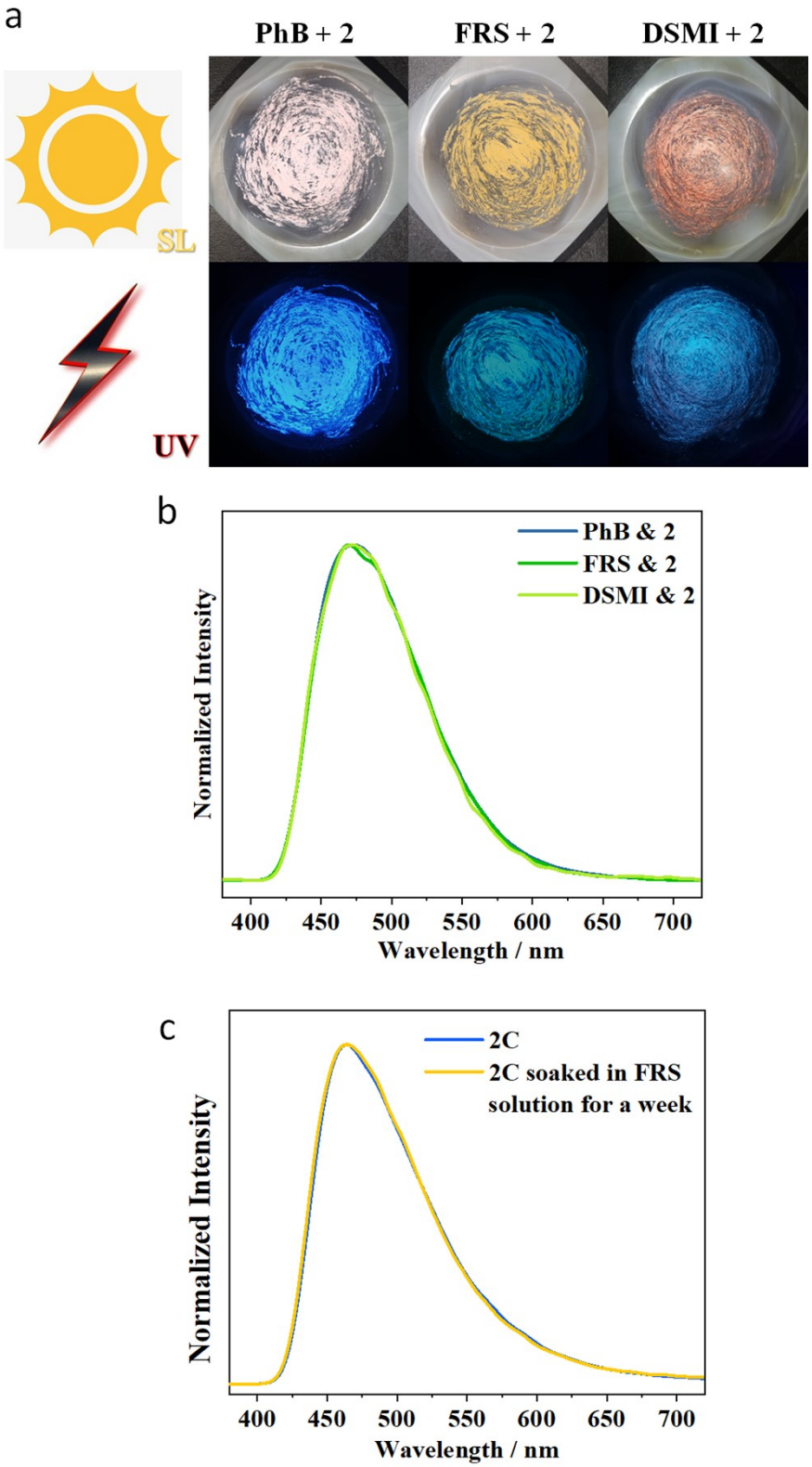

Fig. S19. The photographs under sunlight and a UV lamp (λ_{ex}= 365nm) (a) and solid-state PL spectra (b) (λ_{ex} = 365 nm) of thoroughly ground mixtures of **2** + dye (weight ratio of 50:1). (c) Normalized emission spectra of **2C** and a sample prepared by soaking **2C** in 0.001 M FRS for one week.

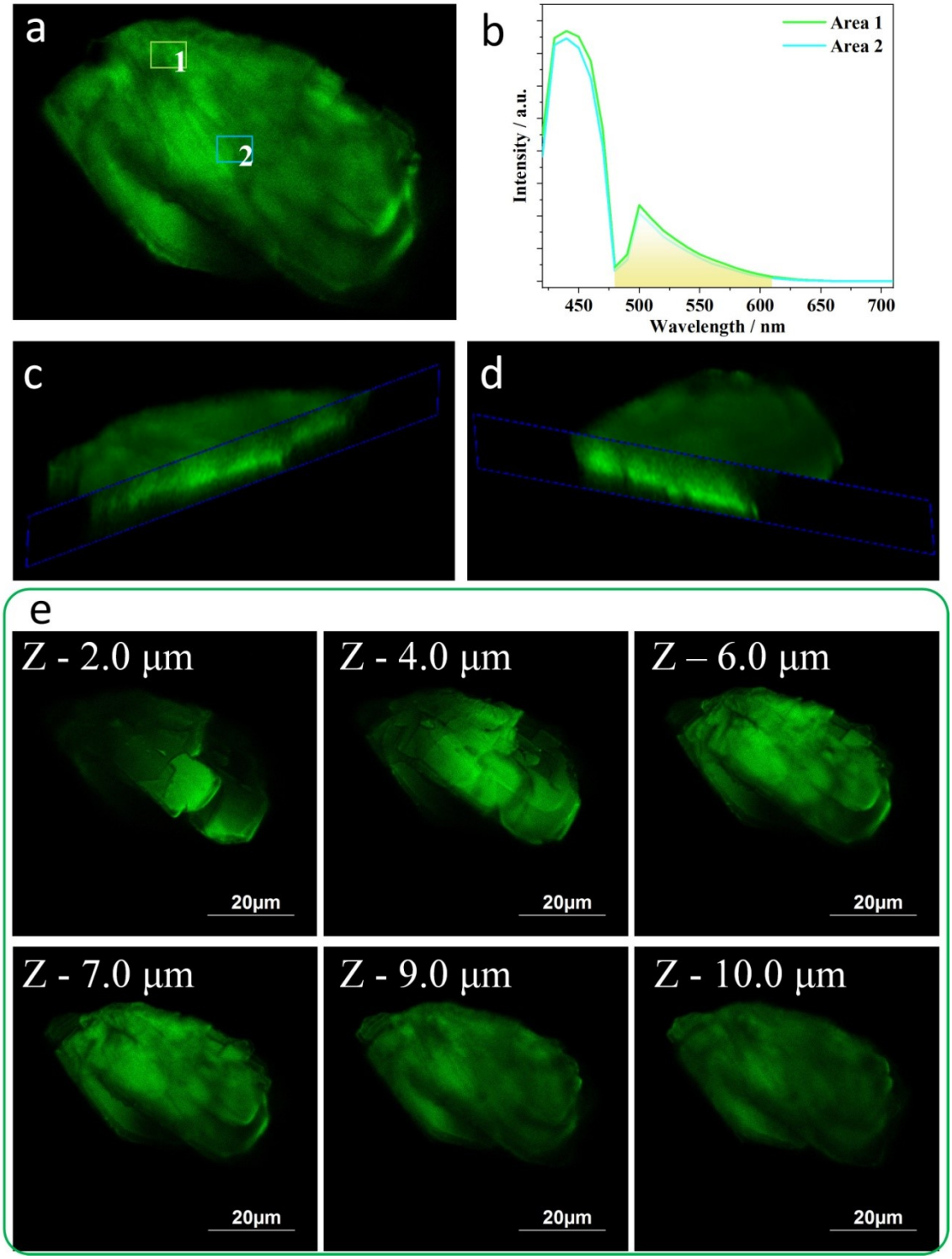

Fig. S20 Confocal scanning images of FRS2@**2C**. (a) Imaged under lambda (wavelength) scan mode (λ = 420-710 nm) for FRS2@**2C**, (b) Luminescence spectra of two selected regions for FRS2@**2C**, (c) and (d) Along different directions, imaged under lambda (wavelength) scan mode (λ=420-710 nm) of the different cross-sections of the crystal for FRS2@**2C**, (e) Depth scan mode collected at the wavelength of 420-710 nm for FRS2@**2C**.

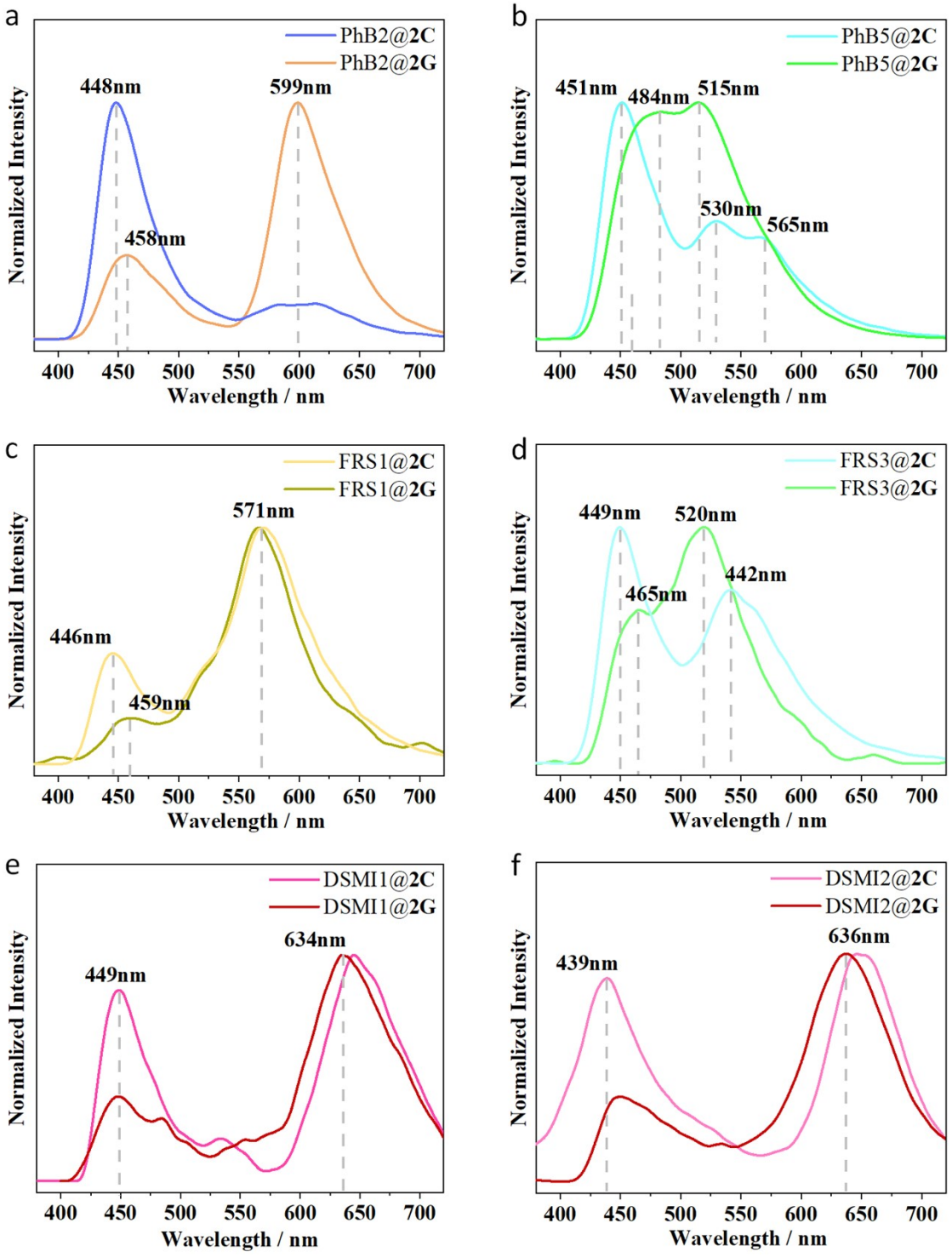

Fig. S21. Solid-state emission spectra of the fresh and ground samples for PhB2@**2** (a); PhB5@**2** (b) ; FRS1@**2** (c) ; FRS3@**2** (d); DSMI1@**2** (e) and DSMI3@**2** (f) (λ_{ex} = 365 nm).

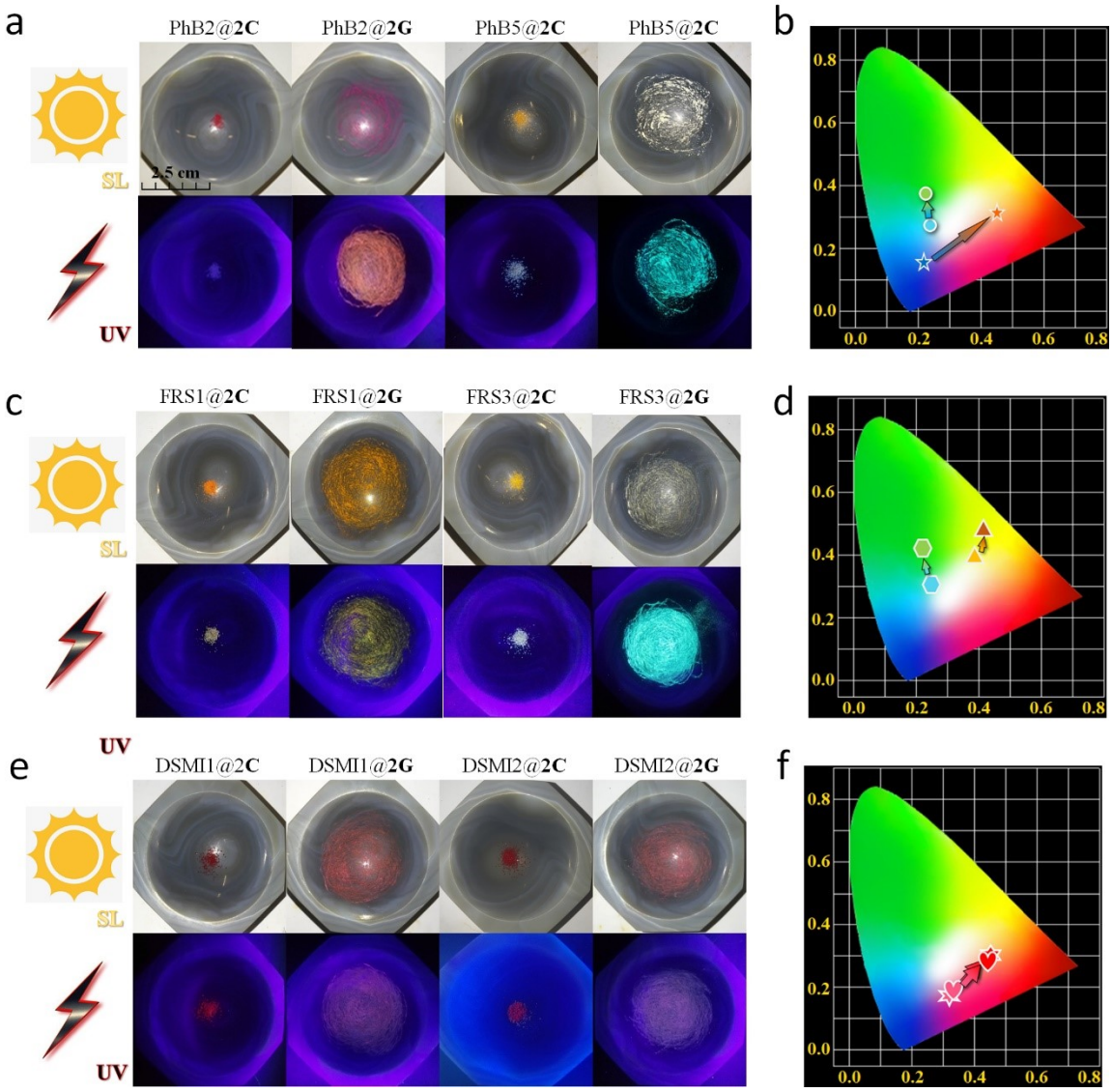

Fig. S22. (a) Photographs of PhB2@**2** and PhB5@**2** before and after grinding under sunlight and a 365 nm UV lamp. (b) The corresponding change of CIE coordinates during the processes of PhB2@**2C**→ PhB2@**2G** and PhB52@**2C**→ PhB5@**2G**. (c) Photographs of FRS1@**2** and FRS3@**2** before and after grinding under sunlight and a 365 nm UV lamp. (d) The corresponding change of CIE coordinates during the processes of FRS1@**2C**→ FRS1@**2G** and FRS3@**2C**→ FRS3@**2G**. (e) Photographs of DSMI1@**2** and DSMI2@**2** before and after grinding under sunlight and a 365 nm UV lamp. (f) The corresponding change of CIE coordinates during the processes of DSMI1@**2C**→ DSMI1@**2G** and DSMI2@**2C**→ DSMI2@**2G**.

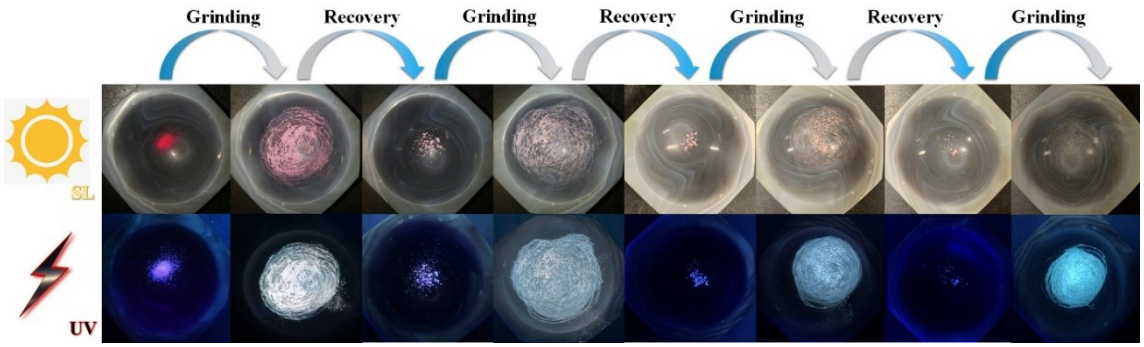

Fig. S23. Photographs of PhB3@**2** upon grinding and fuming by H_2O vapor for several cycles under daylight and a 365 nm UV lamp.

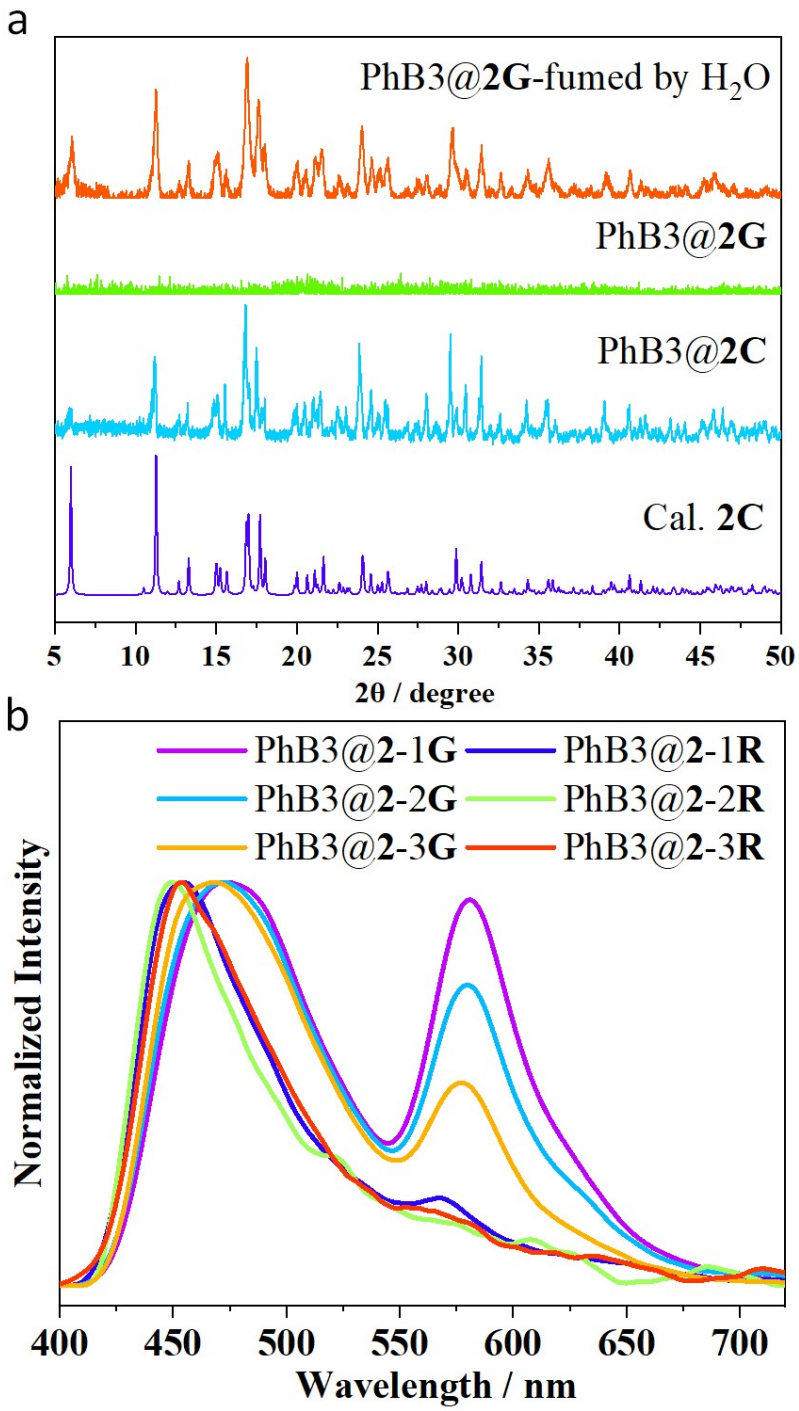

Fig. S24. (a) PXRD of PhB3@**2** during the grinding-recovery process. (b) Photoluminescence of PhB3@**2** during the grinding-recovery process for several cycles (λ_{ex}= 365 nm).

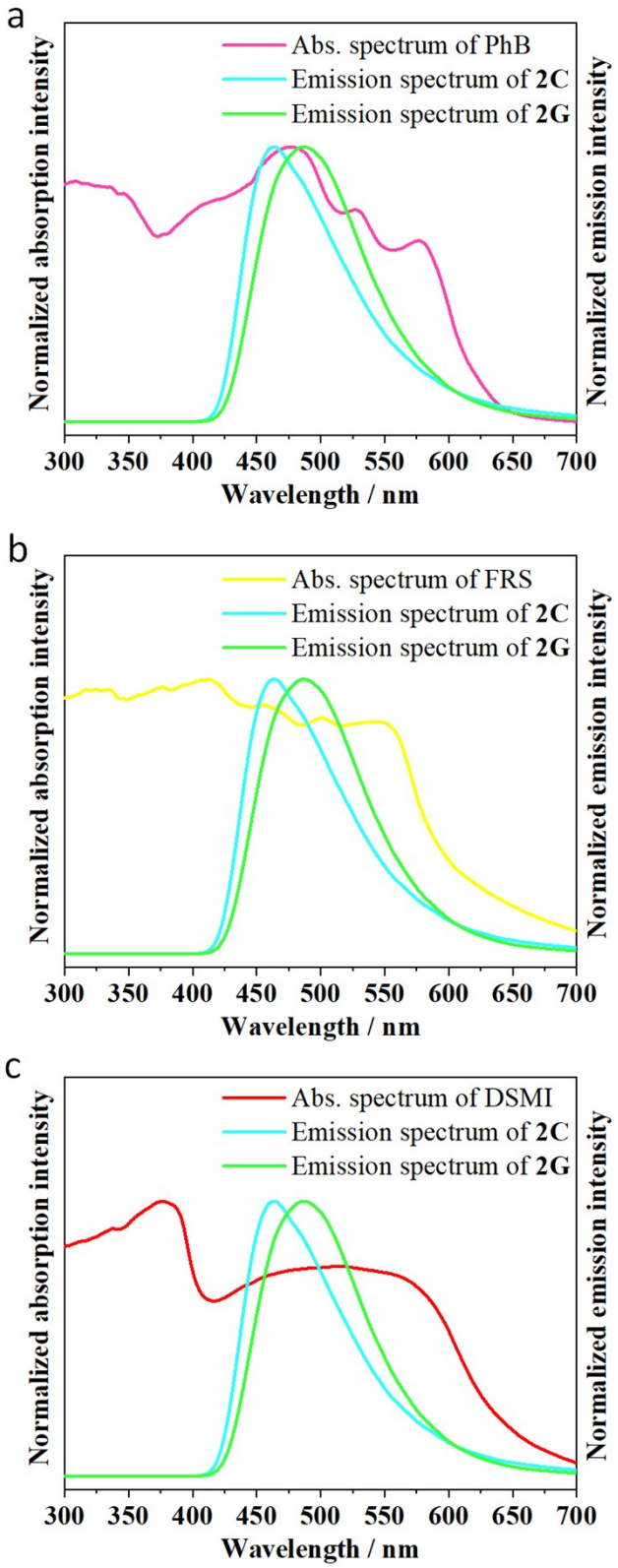

Fig. S25. Spectral overlaps between the emission spectra of **2C** and **2G** and the solid state reflection spectra of PhB (a), FRS (b) and DSMI (c).

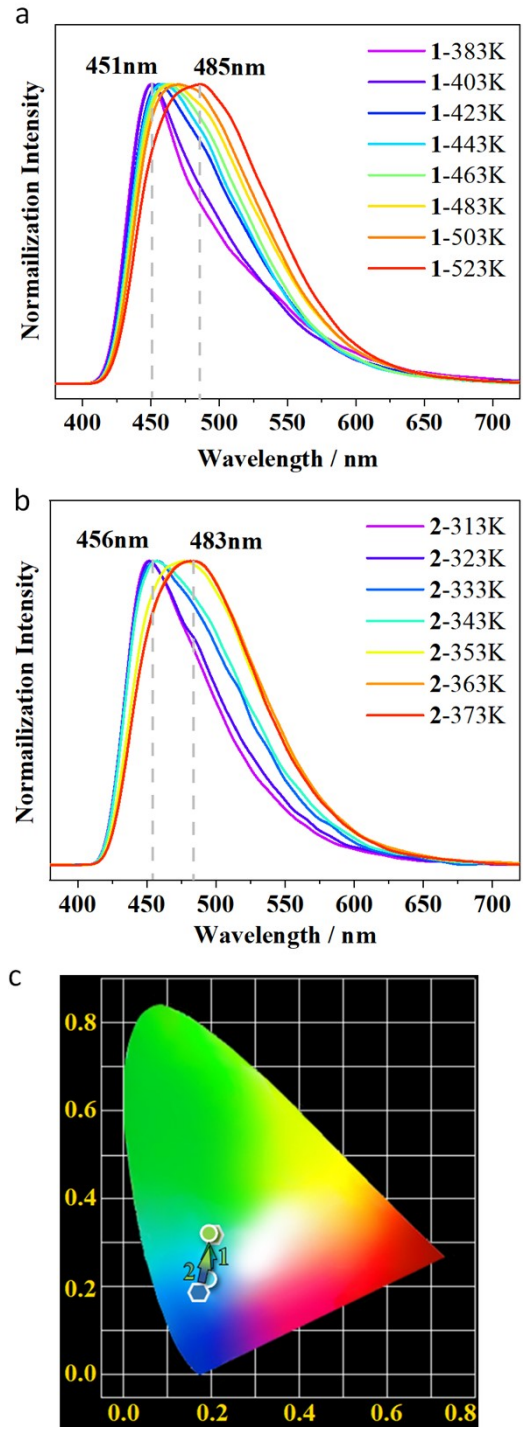

Fig. S26. (a) Emission spectra of **1C** recorded between 383K-523K (λ_{ex}= 365 nm). (b) Emission spectra of **2C** recorded between 313K-373K (λ_{ex}= 365 nm). (c) The corresponding change of CIE coordinates during the heating processes. 1 and 2 show the CIE coordinates change during the heating processes of **1C** and **2C** respectively.

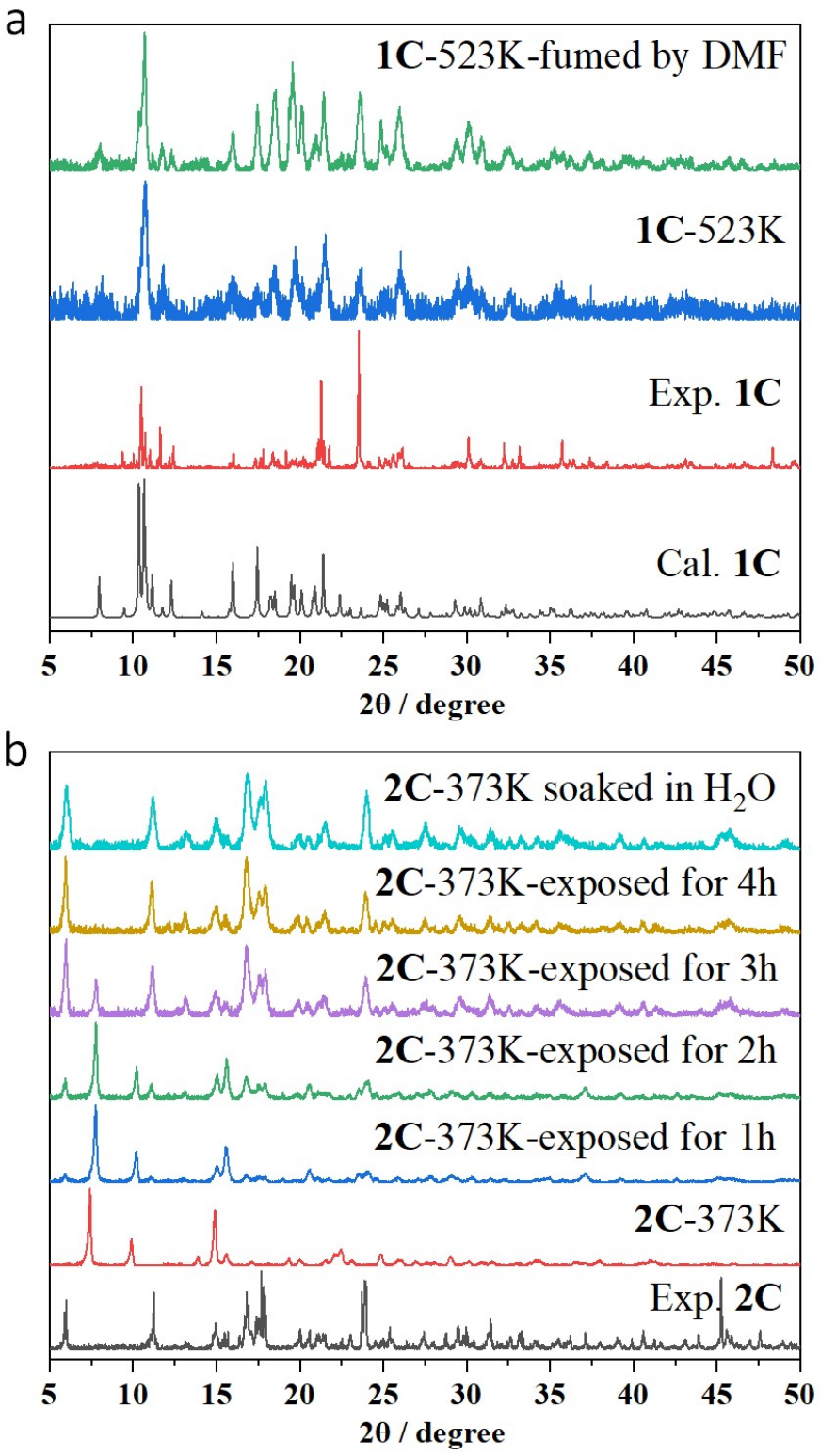

Fig. S27. PXRD pattern of **1C** (a) and **2C** (b) during the heating and recovery processes.

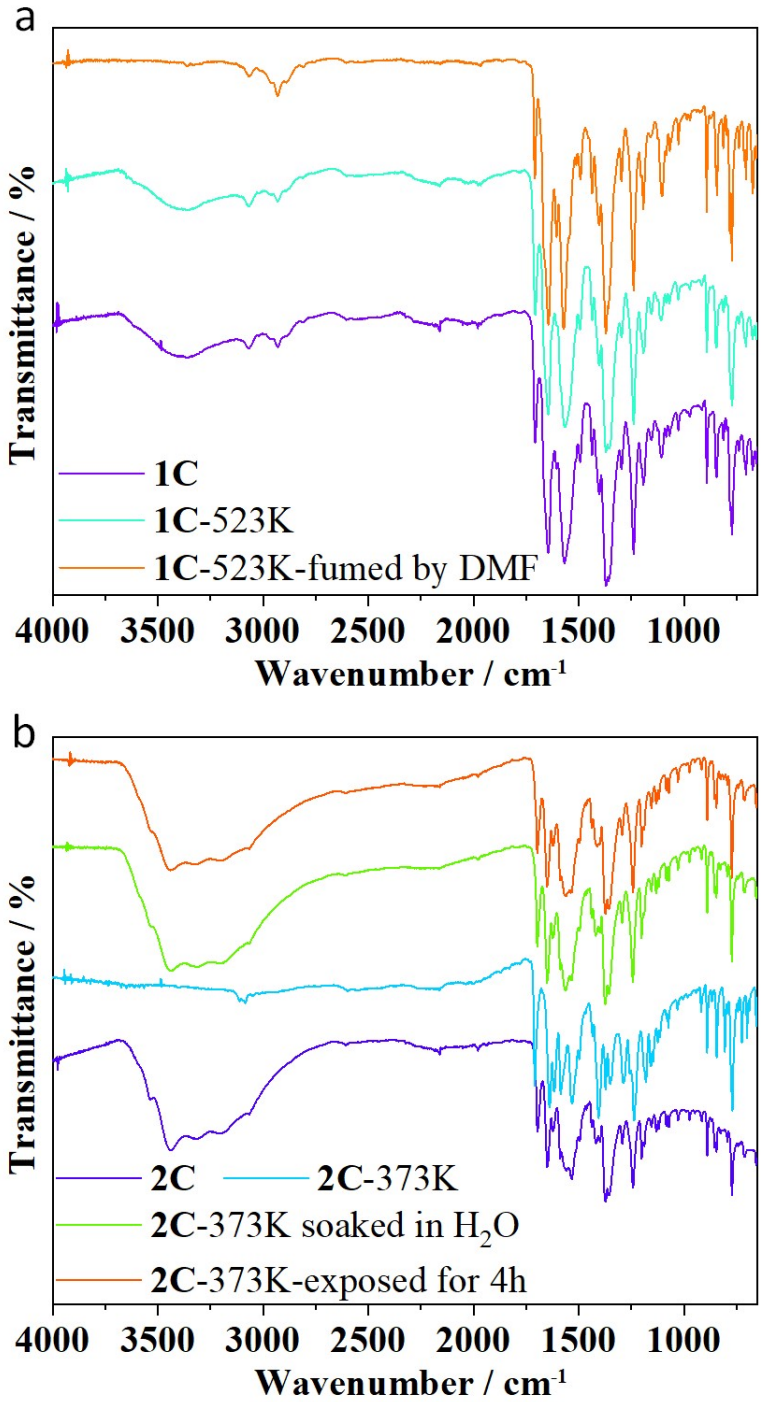

Fig. S28. IR spectra of **1C** (a) and **2C** (b) during the heating and recovery processes.

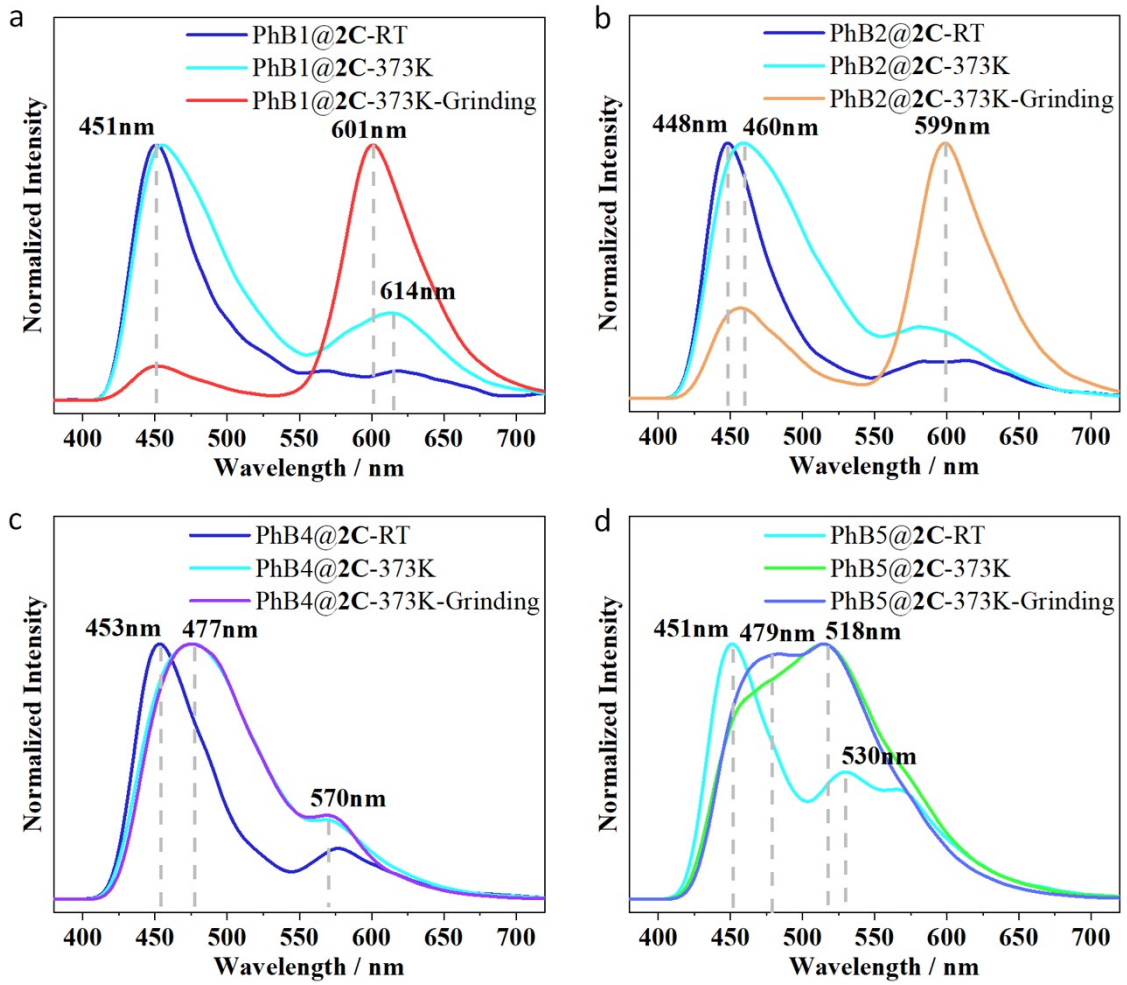

Fig. S29. A comparison of emission spectra of PhB1@**2C** (a), PhB2@**2C** (b), PhB4@**2C** (c) and PhB5@**2C** (d) before and after heating, then grinding.

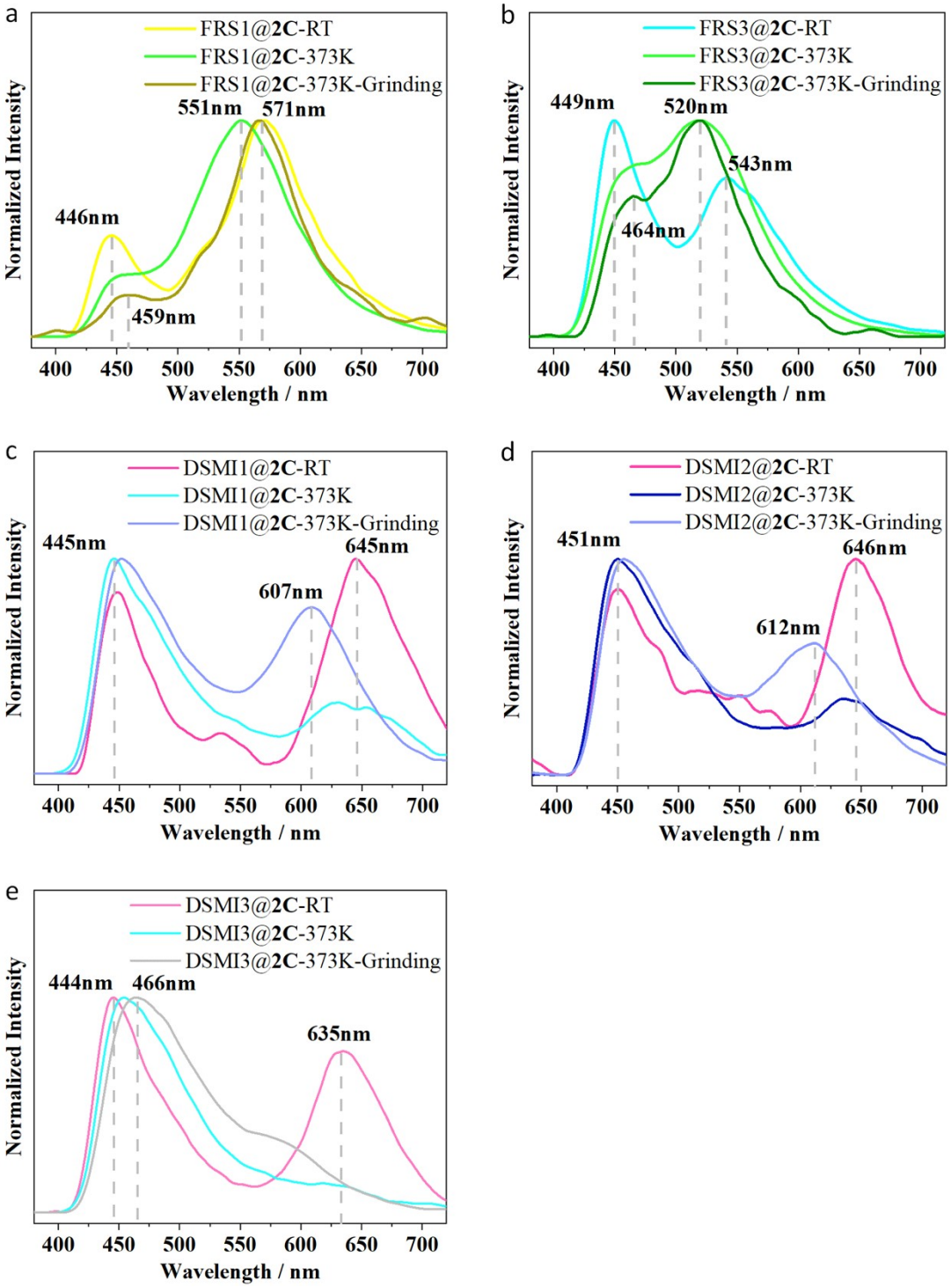

Fig. S30. A comparison of emission spectra of FRS1@**2C**(a), FRS3@**2C**(b), DSMI1@**2C**(c), DSMI2@**2C**(b), and DSMI3@**2C**(d) before and after heating, then grinding.

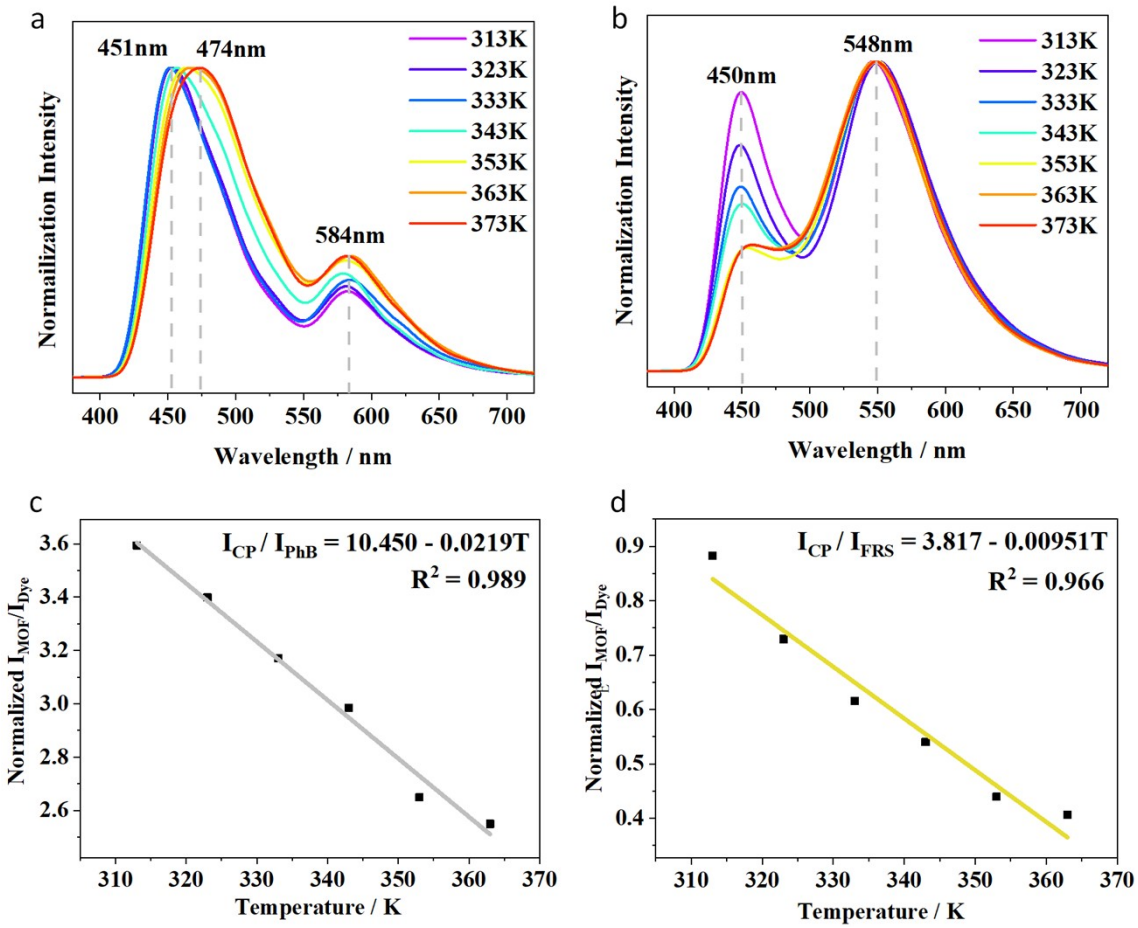

Fig. S31. Emission spectra of PhB3@**2C** (a) and FRS2@**2C** (b) recorded from 313 to 373 K, excited at 365 nm. Temperature-dependent intensity ratio of MOF to dye and the fitted curve for PhB3@**2C** (c) and FRS2@**2C** (d).

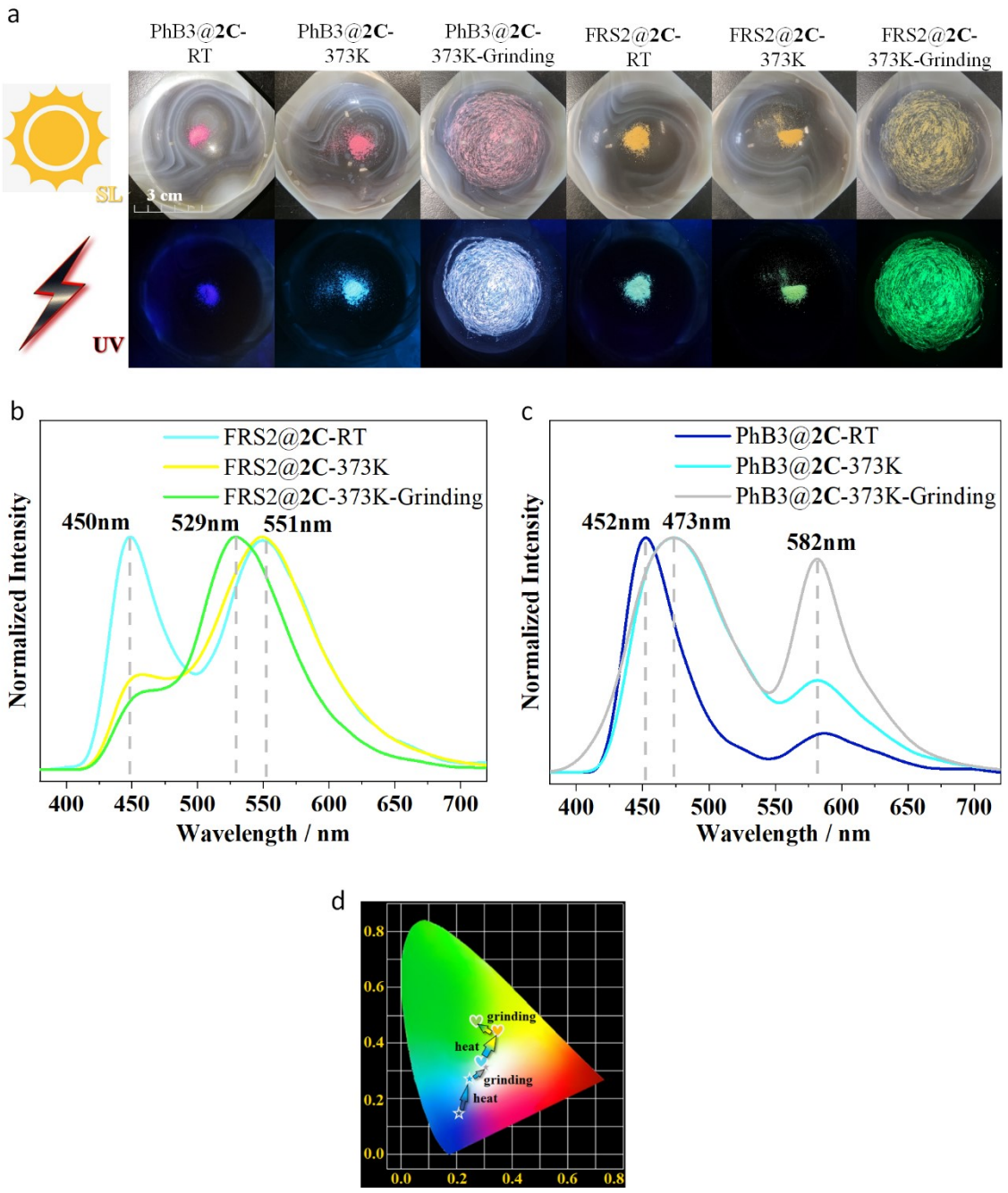

Fig. S32. (a) Photographs of PhB3@**2C** and FRS2@**2C** before and after heat, and after heat-grind under sunlight and a 365 nm UV lamp. (b) Emission spectra of FRS2@**2C** before and after heat, and after heat-grind. (c) Emission spectra of PhB3@**2C** before and after heat, and after heat-grind. (d) The corresponding changes of CIE coordinates during the stimulation processes

3. Supplementary Tables

Tab. S1 Crystallographic data for complexes **1**-**2**.

	1	**2**
Formula	$C_{26}H_{23}CdN_3O_8$	$C_{20}H_{17}CdNO_{10}$
Formula weight	617.87	543.74
Crystal system	Monoclinic	Triclinic
Space group	$P2_1/c$	P-1
a (Å)	10.4784(5)	7.8998(6)
b (Å)	15.0376(8)	8.4895(6)
c (Å)	16.5375(9)	14.9260(12)
α (°)	90	83.087(3)
β (°)	97.530(2)	83.910(3)
γ (°)	90	85.929(2)
V (Å^3)/ *Z*	2583.3(2)/4	986.41(13)/2
D_{calcd} (g /cm^3)	1.589	1.831
μ(mm^{-1})	0.900	1.169
F(000)	1248	544
ϑ range(°)	2.179- 24.404	2.421 -25.000
Reflections collected / unique	38206 / 4233	35204 / 3470
R(int)	0.0355	0.0493
GOF on F^2	1.051	1.060
R_1[a], $I>2\sigma(I)$ (all)	0.0621 (0.0711)	0.0257 (0.0299)
wR_2[b], $I>2\sigma(I)$ (all)	0.1876 (0.1965)	0.0652 (0.0666)
Max/mean shift in final cycle	0.001/0.000	0.003/0.000

[a]$R=\sum(||F_o|-|F_c||)/\sum|F_o|$, [b]$Rw=\{\sum w[(F^2_o-F^2_c)]/\sum w[(F^2_o)^2]\}^{0.5}$, $w = [\sigma^2(F^2_o) + (aP)^2+bP]^{-1}$, where $P = (F^2_o + 2F^2_c)/3$.]. **1**, *a* = 0.1349, *b* = 6.2835. **2**, *a* = 0.0364, *b* = 1.2204.

Tab. S2 Bond lengths (Å) and angles (°) for **1**.

Bond	Dist	Bond	Dist
Cd(1)-O(26)	2.173(4)	Cd(1)-O(23)#2	2.459(5)
Cd(1)-O(25)#1	2.224(4)	O(24)-Cd(1)#3	2.277(5)
Cd(1)-O(24)#2	2.277(5)	O(23)-Cd(1)#3	2.458(5)
Cd(1)-O(28)	2.275(6)	O(25)-Cd(1)#1	2.224(4)
Cd(1)-O(27)	2.368(6)		
Angle	(°)	Angle	(°)
O(26)-Cd(1)-O(25)#1	115.02(18)	O(24)#2-Cd(1)-O(27)	89.3(2)
O(26)-Cd(1)-O(24)#2	152.4(2)	O(28)-Cd(1)-O(27)	179.1(3)
O(25)#1-Cd(1)-O(24)#2	91.34(17)	O(26)-Cd(1)-O(23)#2	98.46(17)
O(26)-Cd(1)-O(28)	96.5(3)	O(25)#1-Cd(1)-O(23)#2	146.15(15)
O(25)#1-Cd(1)-O(28)	89.9(3)	O(24)#2-Cd(1)-O(23)#2	54.82(16)
O(24)#2-Cd(1)-O(28)	91.3(3)	O(28)-Cd(1)-O(23)#2	91.2(2)
O(26)-Cd(1)-O(27)	82.7(2)	O(27)-Cd(1)-O(23)#2	88.6(2)
O(25)#1-Cd(1)-O(27)	90.8(2)		

Symmetry transformations used to generate equivalent atoms:

#1: -x+1, -y+1, -z+1; #2: x+1/2, -y+1/2, z-1/2; #3: x-1/2, -y+1/2, z+1/2.

Tab. S3 Bond lengths (Å) and angles (°) for **2**.

Bond	Dist	Bond	Dist
Cd(1)-O(2)	2.2750(19)	Cd(1)-O(3)#1	2.515(2)
Cd(1)-O(4)#1	2.2844(19)	Cd(1)-O(1)	2.577(2)
Cd(1)-O(8)	2.292(2)	O(3)-Cd(1)#2	2.515(2)
Cd(1)-O(7)	2.314(2)	O(4)-Cd(1)#2	2.2844(19)
Cd(1)-O(9)	2.342(2)		
Angle	(°)	Angle	(°)
O(2)-Cd(1)-O(4)#1	148.73(7)	O(4)#1-Cd(1)-O(3)#1	54.30(7)
O(2)-Cd(1)-O(8)	82.40(8)	O(8)-Cd(1)-O(3)#1	84.97(8)
O(4)#1-Cd(1)-O(8)	82.87(7)	O(7)-Cd(1)-O(3)#1	83.27(8)
O(2)-Cd(1)-O(7)	104.85(8)	O(9)-Cd(1)-O(3)#1	133.64(7)
O(4)#1-Cd(1)-O(7)	95.58(8)	O(2)-Cd(1)-O(1)	53.45(7)
O(8)-Cd(1)-O(7)	166.48(8)	O(4)#1-Cd(1)-O(1)	156.66(7)
O(2)-Cd(1)-O(9)	76.02(7)	O(8)-Cd(1)-O(1)	98.34(7)
O(4)#1-Cd(1)-O(9)	83.07(7)	O(7)-Cd(1)-O(1)	77.79(7)
O(8)-Cd(1)-O(9)	109.23(8)	O(9)-Cd(1)-O(1)	117.85(7)
O(7)-Cd(1)-O(9)	83.82(8)	O(3)#1-Cd(1)-O(1)	102.45(6)
O(2)-Cd(1)-O(3)#1	150.30(7)		

Symmetry transformations used to generate equivalent atoms:

#1: x-1, y+1, z; #2: x+1, y-1, z.

Tab. S4 Hydrogen bond lengths (Å) and bond angles (°) for **2**.[a]

D–H···A	d(D–H)	d(H···A)	d(D···A)	∠DHA	Symmetry code for the acceptor atom
O(7)–H(7A)···O(10)	0.838(10)	2.160(18)	2.953(4)	158(4)	
O(7)–H(7B)···O(4)	0.841(10)	1.849(15)	2.654(3)	160(4)	-x+1, -y+1, -z+2
O(8)–H(8A)···O(6)	0.843(10)	2.001(14)	2.823(3)	165(4)	x-1, y, z
O(8)–H(8B)···O(10)	0.847(10)	1.978(12)	2.812(3)	168(3)	x-1, y, z
O(9)–H(9A)···O(2)	0.846(10)	1.929(12)	2.767(3)	170(3)	-x, -y+1, -z+2
O(9)–H(9B)···O(7)	0.848(10)	2.21(2)	2.936(3)	143(3)	-x, -y+2, -z+2

[a] D, donor atom; A, acceptor atom.

Tab. S5 A summary of the luminescence lifetimes of **1**, **2** and their composities.

Sample name	τ of MOF Emission (ns)	τ of Dye Emission (ns)	Sample name	τ of MOF Emission (ns)	τ of Dye Emission (ns)
H_2L (470 nm)	97.5	/	PhB (628 nm)	/	14.9
FRS (590 nm)	/	11.4	DSMI (661 nm)	/	17.8
1C	76.0	/	**1G**	49.4	/
2C	72.0	/	**2G**	43.1	/
PhB1@**2C**	35.5	14.8	PhB1@**2G**	23.8	17.1
PhB2@**2C**	37.6	15.3	PhB2@**2G**	29.8	19.1
PhB3@**2C**	41.8	18.5	PhB3@**2G**	38.5	20.4
PhB4@**2C**	42.5	19.9	PhB4@**2G**	40.7	19.5
PhB5@**2C**	44.4	22.4	PhB5@**2G**	41.5	12.6
FRS1@**2C**	37.1	19.7	FRS1@**2G**	26.1	18.0
FRS2@**2C**	48.4	13.4	FRS2@**2G**	29.9	12.2
FRS3@**2C**	55.2	11.6	FRS3@**2G**	38.4	9.8
DSMI1@**2C**	40.6	14.8	DSMI1@**2G**	27.4	14.0
DSMI2@**2C**	43.1	14.2	DSMI2@**2G**	32.9	13.0
DSMI3@**2C**	48.1	11.5	DSMI3@**2G**	40.9	10.2

Tas. S6 Quantum efficiency (%) of dye@**2** with different amounts of encapsulated dyes (λ_{ex}=365 nm)

Sample name	Quantum efficiency (%)	Sample name	Quantum efficiency (%)
1C	5.93	**1G**	10.96
2C	6.16	**2G**	16.88
PhB1@**2C**	0.15	PhB1@**2G**	3.32
PhB2@**2C**	0.26	PhB2@**2G**	4.01
PhB3@**2C**	1.02	PhB3@**2G**	11.59
PhB4@**2C**	1.66	PhB4@**2G**	12.38
PhB5@**2C**	2.34	PhB5@**2G**	13.98
FRS1@**2C**	0.54	FRS1@**2G**	2.75
FRS2@**2C**	1.42	FRS2@**2G**	9.43
FRS3@**2C**	1.69	FRS3@**2G**	10.25
DSMI1@**2C**	0.09	DSMI1@**2G**	2.51
DSMI2@**2C**	0.13	DSMI2@**2G**	4.34
DSMI3@**2C**	0.83	DSMI3@**2G**	10.66

Tab. S7 Energy transfer efficiency (%) for **2** with different amounts of encapsulated dyes.

Sample name	Energy transfer efficiency (%)	Sample name	Energy transfer efficiency (%)
PhB1@**2C**	50.63	PhB1@**2G**	44.73
PhB2@**2C**	47.79	PhB2@**2G**	30.79
PhB3@**2C**	41.95	PhB3@**2G**	10.54
PhB4@**2C**	40.88	PhB4@**2G**	5.46
PhB5@**2C**	38.24	PhB5@**2G**	3.62
FRS1@**2C**	48.50	FRS1@**2G**	39.41
FRS2@**2C**	32.75	FRS2@**2G**	30.52
FRS3@**2C**	23.29	FRS3@**2G**	10.89
DSMI1@**2C**	43.51	DSMI1@**2G**	36.39
DSMI2@**2C**	40.12	DSMI2@**2G**	23.57
DSMI3@**2C**	33.10	DSMI3@**2G**	5.13

4. Description of information encryption

Before information encryption, we need to customize two secret keys, which are independent of each other. The first secret key is a table of correspondence between numbers and letters. The second secret key: randomly set a matrix A, and the matrix A satisfies |A|≠0, that is, the matrix A is reversible (Fig. S33).

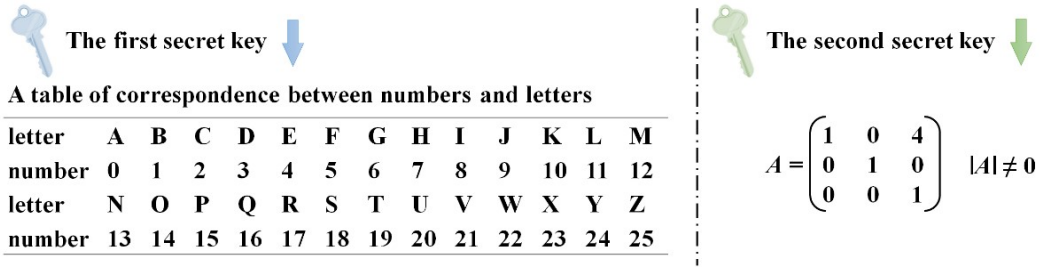

Fig. S33. Schematic diagram of the first and second secret keys.

After the definition of the two secret keys are complete, we take the plaintext message "I agree" as an example, and the encryption process is shown in Fig. 6. The first secret key is used to convert the letters in the plaintext information into numbers and generate a 2×3 matrix P. Then the second secret key, the matrix A is used to multiply the matrix P, and the result is set to matrix B. Finally, take the remainder of 26 for each number in matrix B to obtain matrix C, which is the final ciphertext message (Fig. S34). This is the first encryption process.

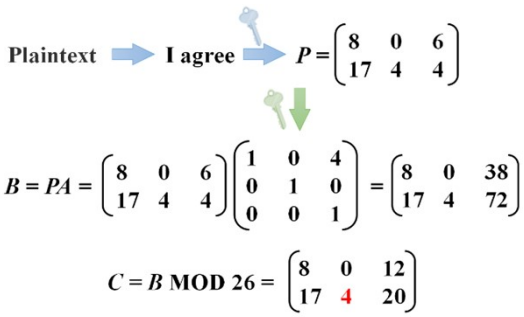

Fig. S34. Schematic diagram of the plaintext encryption process

Then, we need to define the third secret key. using different numbers to represent the luminescence colour change of dye@**2** under different treating processes (Fig. S35), and these numbers come from matrix C, as shown in Fig. 6. According to the position of the number in the matrix C, different composites are glued on the sticky black tape to make an encrypted map, which is used to replace encrypted ciphertexts. This is the second encryption method.

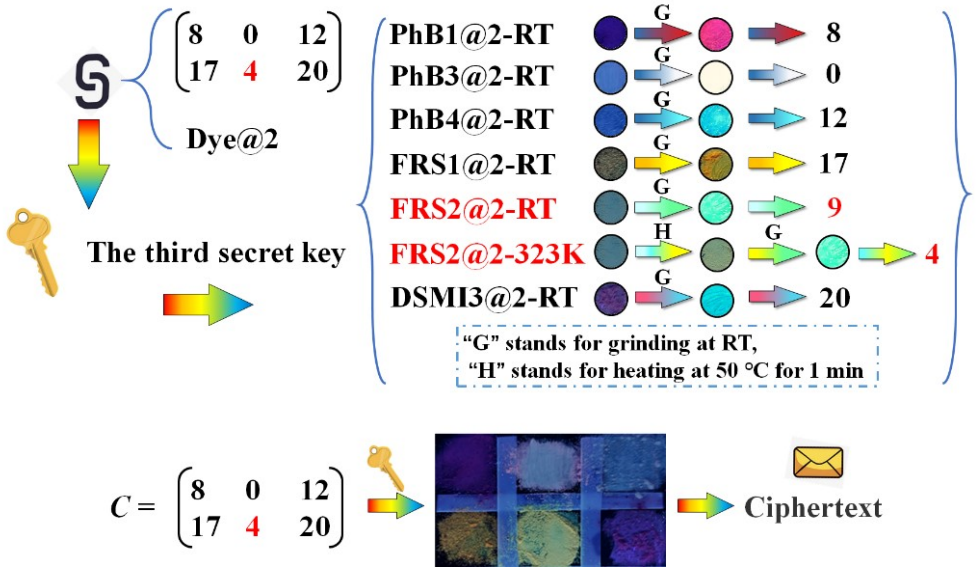

Fig. S35. Schematic diagram of the third secret key.

It should be noted that among the six used composites, only FRS2@**2C** has a significant luminescence colour change after being heated at 323K for 1 min, while those of other composites do not change significantly under the same stimulus. Therefore, the different treatment processes of FRS2@**2C**, being directly ground (process 1 in Fig. 6) or first being heated and then ground (process 2 in Fig. 6), will cause different luminescence colour changes of the composite in the encrypted map, that is, different ciphertext information (Fig. S36). Thus the special TL property of FRS2@**2C** is used for the third encryption process.

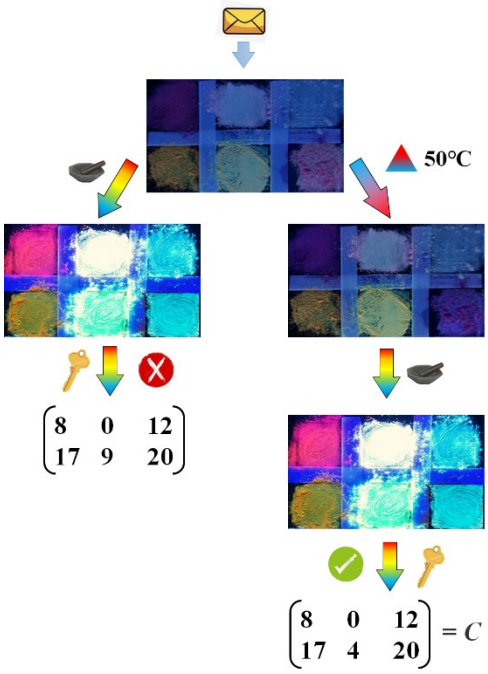

Fig. S36. Schematic diagram of different encrypted ciphertexts obtained though different treating process of FRS2@**2C** in the encrypted map.

In the decryption process, first, the encrypted map needs to be heated at 323K for 1 min and then ground to observe the luminescence colour changes of the composites in each square of the encrypted map. According to the content of the third key, the number represented by each composite is obtained, and the ciphertext message, namely matrix C, can be obtained. Second, the second secret key is used to calculate the inverse matrix A^{-1} of matrix A. Multiply the matrix C and the inverse matrix A^{-1}, and take the remainder of 26 for each number in the resulting matrix, the matrix P can be obtained. Third, the first secret key is used to convert the numbers in the matrix P into the corresponding letters, and the plaintext message "I agree" can be obtained (Fig. S37).

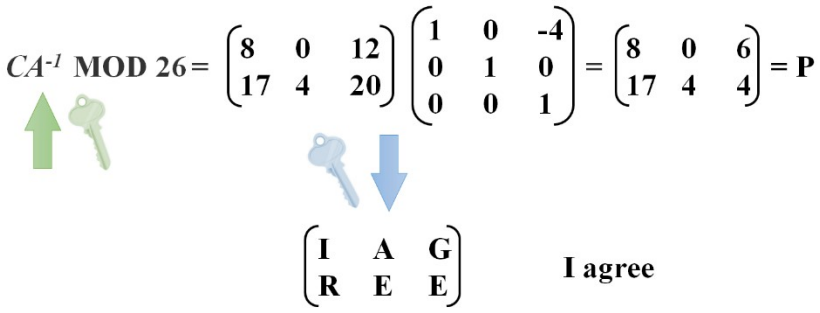

Fig. S37. Schematic diagram of the decryption process of encrypted ciphertext

References

[1] D. Singh, P.K. Bhattacharyya, J.B. Baruah, *Cryst. Growth Des.*, 2009, **10**, 348-356.

[2] G.M. Sheldrick, *Acta Crystallogr., Sect. A: Found. Crystallogr.*, 2015, **A71**, 3-8.